NATIONAL TRANSPORTATION SAFETY BOARD
Office of Research and Engineering
Vehicle Performance Division
Washington, D.C. 20594

May 9, 2016

Finite Element Modeling Study Report

A. ACCIDENT INFORMATION

Place	:	Valhalla, New York
Date	:	February 3, 2015
Vehicle #1	:	2011 Mercedes ML350
Vehicle #2	:	Metro-North passenger train #659
NTSB No.	:	DCA15MR006
Investigator	:	Michael Hiller

B. TOPICS ADDRESSED

Finite element (FE) modeling was used to examine the stresses and deformation modes in the third rail assembly under assumed loading scenarios.

C. DETAILS OF THE STUDY

A 3-D finite element model of the third rail assembly was constructed based on design drawings. Hypothetical loads and boundary conditions simulating deformations that the assembly may have experienced during the accident were applied to the model. The study focused on the stresses in the assembly that may lead to failure of the assembly. The FE modeling was carried out using the FE software Abaqus version 6.14 and 2016.

1. Geometry

The model of the third rail assembly includes the third rail, the third rail splice plate and the bolt hardware. Figure 1 shows the modeled geometry. Half of the assembly was modeled to take advantage of the symmetry of the structure. The design drawing that the geometry was based on is shown in Figure 2.

a. Third rail

A 4-ft segment of the third rail was modeled, as shown in Figure 3.

b. Third rail splice plates

The geometry of the third rail splice plates is shown in Figure 4. Features such as fillets were included in the geometry. Dimensions were rounded up by 1/32 inch.

c. Bolt hardware

The bolt hardware geometry is shown in Figure 5. It includes as one solid part the oval neck track bolt, the washer and the nut. The nut geometry was approximated as a cylinder. No thread geometry was included for either the bolt or the nut.

2. Material

The splice plate material was specified as cast malleable iron ASTM A-47. A bilinear elastic-plastic material model was created for this material based on literature data. The Young's modulus was 29,000 ksi and the Poisson's ratio was 0.3. The yield stress was 35 ksi, the ultimate tensile stress was 53 ksi and the ultimate strain was 0.18. The bolt material was specified as ASTM A183 Grade 2 steel. Similar to the splice plate material, a bilinear elastic-plastic material model was created for the bolt material. The Young's modulus and Poisson's ratio were the same as the splice plate material. The yield stress was 80 ksi, the ultimate tensile stress was 110 ksi and the ultimate strain was 0.12. For both materials, perfectly plastic behavior was assumed past the ultimate strength. Figure 6 shows the engineering stress-strain curves of the two materials. Abaqus uses true stress and true strain as stress and strain measures. Figure 7 shows the true stress-strain curves of the two materials. True stress and strain are used in subsequent sections. The rail material was approximated as linear elastic with the same modulus and Poisson's ratio as the other materials. This approximation was based on the fact that inelastic behavior of the rail was not of interest of this study.

3. Interfacial Conditions

a. Splice plate-Rail interface

Frictional contact conditions were defined between the rail and the upper and lower mating surfaces of the splice plate, as shown in Figure 8. The geometry was such that the surfaces were in perfect contact initially. The friction coefficient was chosen to be 0.3.

b. Splice plate-Bolt interface

Frictional contact conditions similar to those at the splice plate-rail interface were defined between the bolt hardware and the splice plate, as shown in Figure 9. The friction coefficient was chosen to be 0.3.

4. Loads and Boundary Conditions

The model had three loading steps. In the first step simulating installation, a bolt tension of 20 kips was applied to the bolts. The 20 kips magnitude corresponds to approximately 250 ft-lbs bolt torque, which was the value provided by Metro-North Railroad. The bolt tension was applied via Abaqus' assembly load feature. In the second step, a compressive load was applied to the rail as shown in Figure 10. This load was to simulate the force exerted on the rail by the SUV during the accident. Two

values, 9 kips and 40 kips, were considered as potential lower and upper limits of the forces that could have been applied to the rail during the accident. These two values were computed as averaged impact force based on momentum of the train when it struck the SUV. In the third step, the assembly was deformed by applying a rotation to the free end of the rail. Specifically, the free end of the rail was rigidly constrained to a reference point and a rotation was prescribed to the reference point. Two modes of deformation were considered: in-plane bending and out-of-plane bending. These two deformation modes represented possible scenarios from the accident. Figure 11 shows the two considered deformation modes. All loads considered were applied in a quasi-static fashion. Although the actual deformation process from the accident was dynamic, neither transient loading nor rate-dependent material behavior was expected to change the overall deformation mode of the assembly. In all steps symmetric boundary conditions were applied to the symmetry planes of the splice plates, as shown in Figure 10.

5. Mesh

Figure 12 shows the FE mesh on the splice plates. Both plates were shown to provide views from both sides of the mesh. The splice plate was meshed with second order tetrahedral elements (C3D10 in Abaqus). Each splice plate has 80,542 elements in total. Figure 13 shows the mesh on the bolt hardware. The bolt hardware was meshed with first order reduced integration brick elements (C3D8R in Abaqus). Each bolt hardware part has 2,649 elements in total. Figure 14 shows the mesh on the rail. The rail was meshed with second order tetrahedral elements and had 39,443 elements in total. The longitudinal direction of the rail mesh was made coarse to save computational cost. A summary of mesh statistics of the three parts is shown in Table 1. The entire assembly has 205,825 elements and 1,006,142 degrees of freedom in total.

Table 1. Mesh statistics

Part	Total Number of Elements	Typical Mesh Dimension
Splice Plate	80,542	0.11 inch
Bolt hardware	2,649	0.14 inch
Rail	39,443	0.2 inch

6. Output

Model output from each of the loading steps is discussed below. A total of four steps are discussed since the deformation step contained two different modes.

a. Bolt tension step

Figure 15 shows the contours of the Mises stress in the structure's cross section at approximately the centerline of the inner bolt. The peak stress in the bolt was about 60 ksi. The bolt exhibited a bending type of stress distribution with higher stresses on

top and lower stresses at bottom. This was due to the fact that the lower region of the splice plate at this location had less material, hence less stiffness and experienced more deformation. Please refer to figure 2 for details of the splice plate structure. To further demonstrate this effect, figure 16 shows the contours of the effective plastic strain in this cross section. It can be seen that the bottom of the splice plate experienced considerable plastic deformation. As a result, the lower part of the splice plate was pushed more inwardly than the upper part by the bolt tension, causing the bolt to slightly bend upwards.

Figure 17 shows the contours of the Mises stress in the structure's cross section at approximately the centerline of the outer bolt. The peak stress in the bolt was about 45 ksi. Comparing to the inner bolt, the outer bolt showed a more uniform stress distribution and the magnitude is very close to the nominal stress value, which was 45 ksi given the prescribed tension of 20 kips. Figure 18 shows the contours of the effective plastic strain in this cross section. The effective plastic strain in the splice plate was much less than at the inner bolt cross section. This was due to the fact that the splice plate had equal stiffness on the upper and lower regions.

Figure 19 shows the contours of the Mises stress in the splice plates. The peak stress value occurred in local regions where contact happened. Away from those local regions, the stress values were below 40 ksi. Figure 20 shows contours of the effective plastic strain in splice plates. Once again the appreciable plastic strain localized at contact regions. Figure 21 shows the contours of the Mises stress in the portion of the rail close to the spliced end. Except for contact stresses in very localized regions, the stresses in the rail are below 30 ksi.

b. Axial loading step

Figures 22 through 24 show the contours of the Mises stress in the bolts, the splice plates and the rail at the end of the axial loading step for the case with 9 kips axial force. Comparing Figures 22 through 24 to Figures 15 through 21 from the previous step, it can be seen that the stress distributions in the structure change very little under the prescribed axial force.

For the second case considered, figure 25 shows the deformation of the structure, magnified 10 times, under 40 kips axial force. It can be seen that the structure bends slightly under the load. Figure 26 shows the contours of the Mises stress in the bolts, plotted under the same scale as Figure 22. It can be seen that the bolt stresses increased slightly with a higher axial load. Figure 27 shows the contours of the Mises stress in the splice plates, plotted under the same scale as Figure 23. It can be seen that the stresses in the splice plates increased in the region where bending occurred. But higher stresses still are confined to localized contact areas and the stresses away from the contact areas remained below 40 ksi. Figure 28 shows the contours of the Mises stress in the rail. Comparing to the previous case, the higher axial load caused the stresses in the rail to increase in some regions but remain below 30 ksi with the exception of local contact stresses.

c. Deformation step: in-plane bending mode

Figure 29 shows the deformed shape of the in-plane bending mode with low axial force. The image of the structure was mirrored to show the symmetric half and indicate what the total assembly would look like. The simulation was terminated before the top corner of the two rail segments touched each other. At this point, the applied rotation at the free end was 0.075 radian and the relative vertical displacement between the free and the spliced end was 3.6 inches.

Figure 30 shows the free body diagram (FBD) at the spliced end. The force resultant, shown as the red arrow, was mostly in the axial direction and its magnitude was very close to the applied axial force of 9 kips. The moment resultant, shown as the blue arrow, pointed to the lateral direction which was consistent with in-plane bending. The magnitude of the moment was 49 kips-inch, indicating that the structure still had stiffness to resist bending at the prescribed rotation. The curve of moment resultant vs. prescribed rotation is shown in Figure 31. In can be seen that the structure's behavior was ductile under this deformation mode and the structure's stiffness had not degraded to zero at the end of the simulation.

Figure 32 shows the contours of the Mises stress in the splice plates. Values higher than the 62.5 ksi, the ultimate tensile stress in true stress measure, are shown in grey color. Please note that the elastic-plastic material model for the splice material assumed perfect plasticity past the ultimate point. So the Mises stress in an element could never exceed 62.5 ksi. The reason that higher stress values are seen on figure 32 is Abaqus' post-processing approach. In any case, elements rendered with the grey color in figure 32 can be viewed as past the ultimate point and having zero stiffness. From figure 32 it can be seen that the elements that had the highest stresses were at the upper region at the symmetry plane, or at the lower region where there was less material. High stresses in both regions were caused by contact. The only high stresses due to bending of the splice plate were in the fillet area highlighted in figure 32. Figure 33 shows the contours of the effective plastic strain in the splice plates. The upper limit of the plot legend was chosen to be 0.18, the ultimate tensile strain. Similar to the stress plot, the most prominent plastic deformation occurred at contact areas, with the highlighted fillet area also having considerable plastic deformation.

Figure 34 shows the contours of the Mises stress in the bolts. Although the stresses increased from the previous step, they mostly remained below 80 ksi which was the yield stress for the bolt material. Figure 35 shows the contours of the Mises stress in the rail. The peak stress spots on the rail corresponded to areas in contact with the splice plates and their magnitudes were not very high.

Figure 36 shows the FBD at the spliced end for the same deformation mode with the high axial load. Similar to the previous case, the force resultant's direction and magnitude were consistent with the applied axial force. With the high axial load, the prescribed rotation was 0.05 radian when the rail segments were close to touching each other. This value was lower than the case with lower axial load, which made sense as the higher axial load pushed the rail segments closer. The relative vertical displacement

between the free and the spliced end was 2.5 inches. Figure 37 shows the curve of moment resultant vs. prescribed rotation. The same ductile behavior as the previous case was observed. Also, the structure's stiffness had not degraded to zero at the end of the simulation. The magnitude of the moment where the structure's stiffness started to soften was slightly lower than the case with low axial load.

Figure 38 and 39 show the contours of the Mises stress and the effective plastic strain in the splice plates for the case with high axial load. The stresses and plastic deformation in the splice plates were similar to the case with lower axial load. The plastic deformation at the previously identified fillet was slightly lower due to the reduction of tensile stress in the presence of a higher compressive axial load.

Figure 40 and 41 show the contours of the Mises stress in the bolts and in the rail for the case with high axial load. The stresses in the bolts were similar to the case with lower axial load. The stresses in the rail body were slightly higher than the previous case, but the peak stress spots on the rail still corresponded to areas in contact with the splice plates.

d. Deformation step: out-of-plane bending mode

Figure 42 shows the deformed shape of the out-of-plane bending mode with low axial force. The image of the structure was mirrored to show the symmetric half of the assembly. Similar to the in-plane bending mode, the simulation was terminated before the corners of the two rail segments touch each other. At this point, the applied rotation at the free end was 0.047 radian and the relative lateral displacement between the free and the spliced ends was 2.07 inches.

Figure 43 shows the FBD at the spliced end. The force resultant was consistent with the applied axial load of 9 kips. The moment resultant pointed to the vertical direction which was consistent with out-of-plane bending. The magnitude of the moment was 110 kips-inch, indicating that the structure still had stiffness to resist bending at the prescribed rotation. The curve of moment resultant vs. prescribed rotation is shown in Figure 44. It can be seen that the structure's behavior was ductile under this deformation mode and the structure's stiffness had not degraded to zero at the end of the simulation.

Figure 45 shows the contours of the Mises stress in the splice plates. Values higher than the 62.5 ksi, the ultimate tensile stress in true stress measure, are shown in grey color. It can be seen that the elements that had the highest stresses were at the lower region where there was less material, and the high stresses were caused by contact. The only high stresses due to bending of the splice plate were in the area close to the inner bolt hole, as highlighted in figure 45. Figure 46 shows the contours of the effective plastic strain in the splice plates. The upper limit of the plot legend was chosen to be 0.18, the ultimate tensile strain. Similar to the stress plot, the most prominent plastic deformation occurred at contact areas, with the highlighted area near the inner bolt hole also having considerable plastic deformation.

Figure 47 and 48 show the contours of the Mises stress and the effective plastic strain in the bolts. In this deformation mode, the bending of the rail and splice plates caused the bolts to bend as well, hence adding bending stresses on top of the bolt tension. The peak stresses in the bolts were about 87 ksi, exceeding the yield stress. Plastic deformation can be seen developing near the fastened end of the bolts. Figure 49 shows the contours of the Mises stress in the rail. The peak stress spots on the rail corresponded to areas in contact with the splice plates and their magnitudes were not very high. The stresses in the rail body were higher for this bending mode, and the peak stress spots on the rail still corresponded to areas in contact with the splice plates.

Figure 50 shows the FBD at the spliced end for the out-of-plane bending mode with the high axial load. Similar to the previous case, the force resultant's direction and magnitude were consistent with the applied axial force. The moment resultant's direction was not strictly out-of-plane and indicated the presence of an in-plane bending component in this case. With the high axial load, the prescribed rotation was 0.03 radian when the rail segments were close to touch each other. This value was lower than the case with lower axial load, due to the fact that the higher axial load pushed the rail segments closer. The relative vertical displacement between the free and the spliced end was 1.35 inches. Figure 51 shows the curve of moment resultant vs. prescribed rotation. The same ductile behavior as the previous case was observed. Also, the structure's stiffness had not degraded to zero at the end of the simulation. The magnitude of the moment where the structure's stiffness started to soften was considerably lower than the case with low axial load.

Figure 52 and 53 show the contours of the Mises stress and the effective plastic strain in the splice plates for the case with high axial load. The stresses and plastic deformation in the splice plates were similar to the case with lower axial load. Figure 54 and 55 show the contours of the Mises stress and the effective plastic strain in the bolts. The stresses and plastic deformation in the splice plates were similar to the case with lower axial load. Figure 56 shows the contours of the Mises stress in the rail. The stresses in the rail body were slightly higher than the previous case, but the peak stress spots on the rail still corresponded to areas in contact with the splice plates.

D. REFERENCES

1. Design drawing, 150-lb Third Rail Splice Plate and Splice Assembly, Metro-North Railroad, 2005.

Xiaohu Liu
Finite Element Analyst

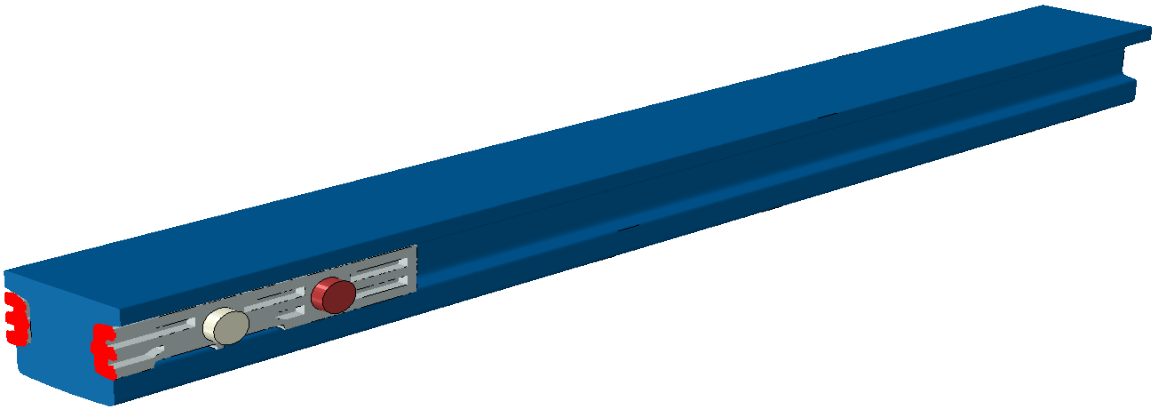

Figure 1. Half symmetry model of the third rail assembly with the symmetry plane highlighted in red.

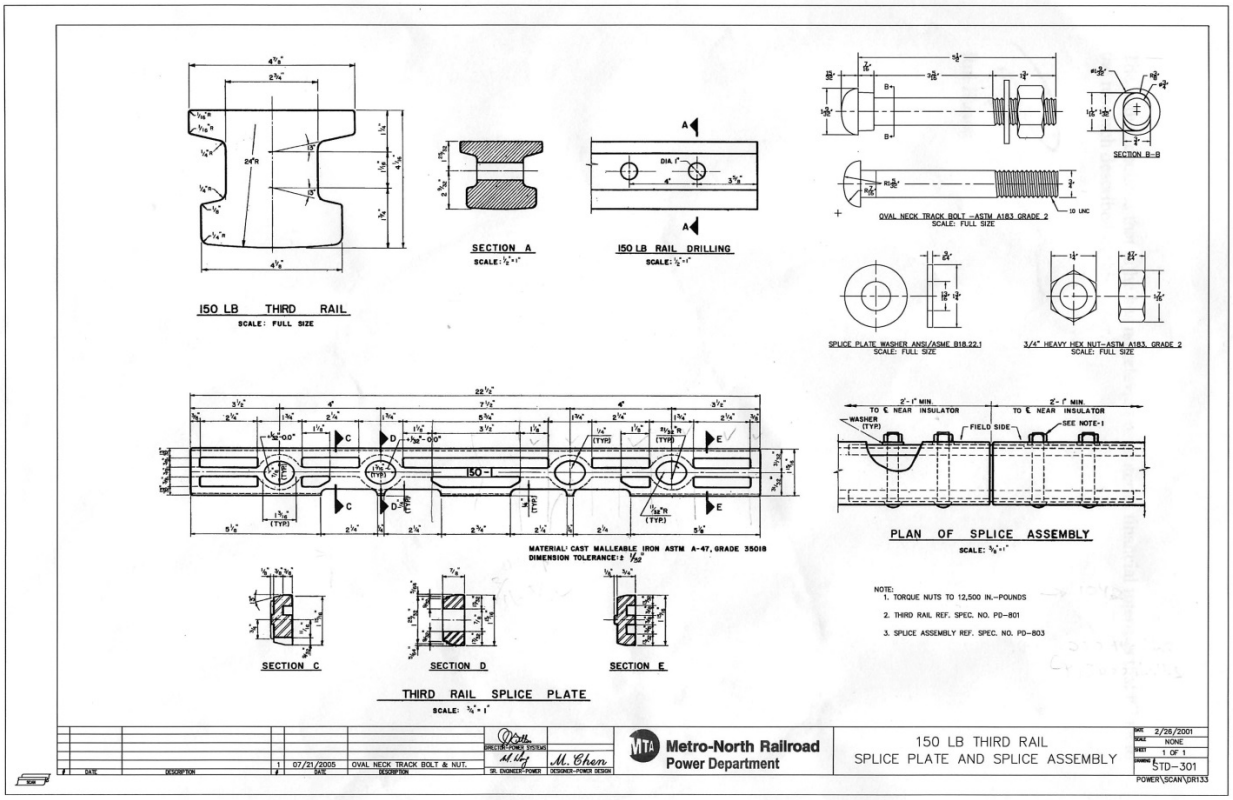

Figure 2. Design drawing of the third rail assembly [Reference 1].

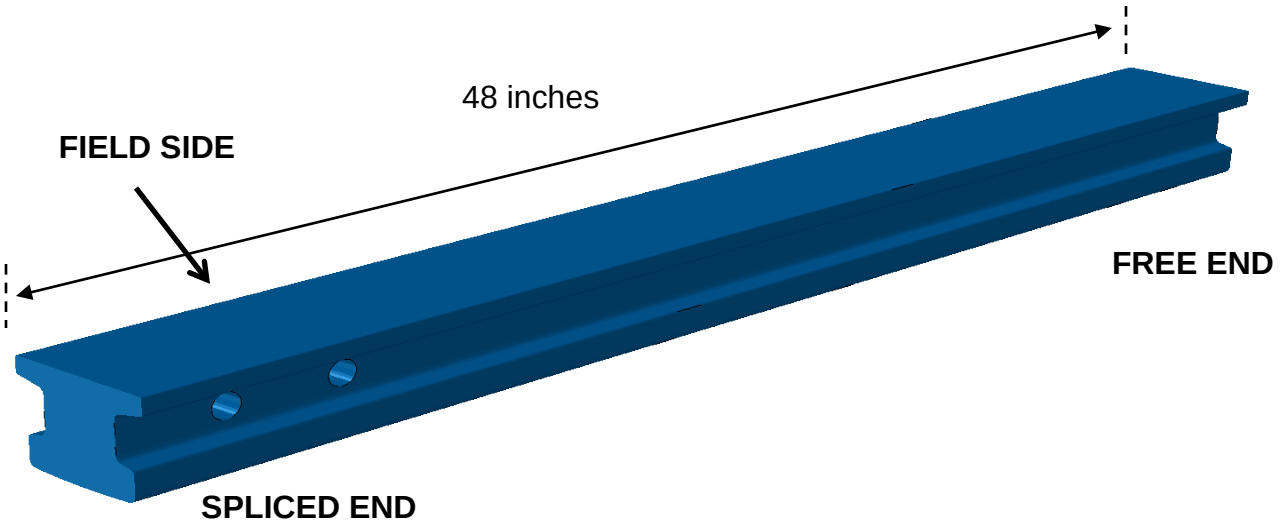

Figure 3. Model geometry of the third rail.

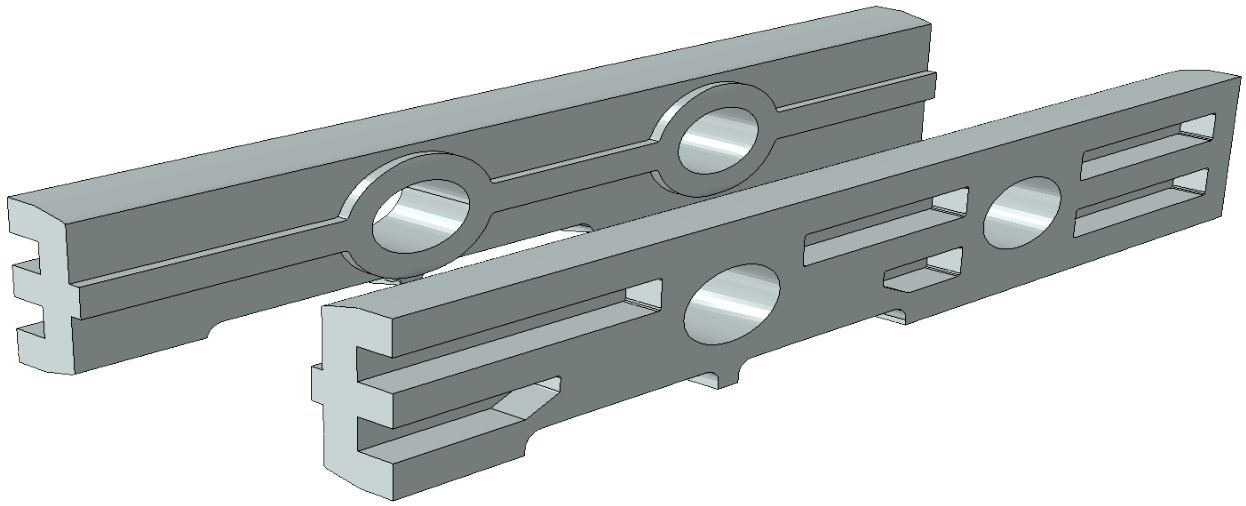

Figure 4. Model geometry of the splice plates.

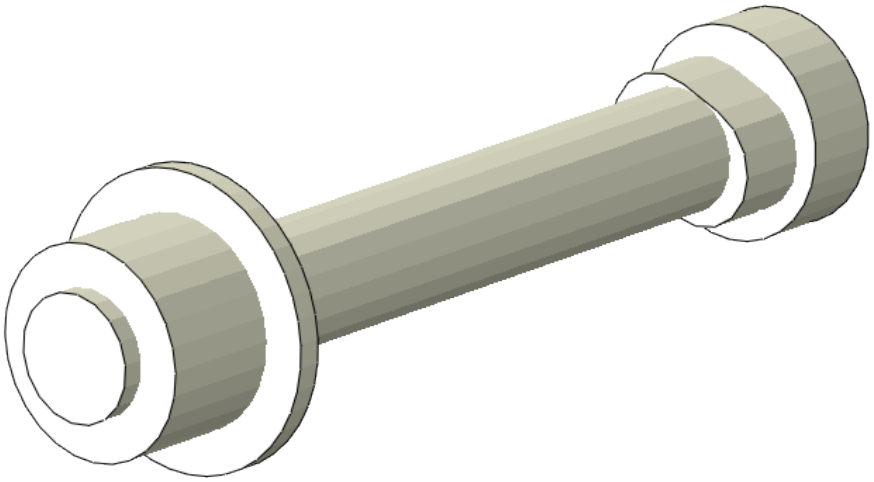

Figure 5. Model geometry of the bolt hardware.

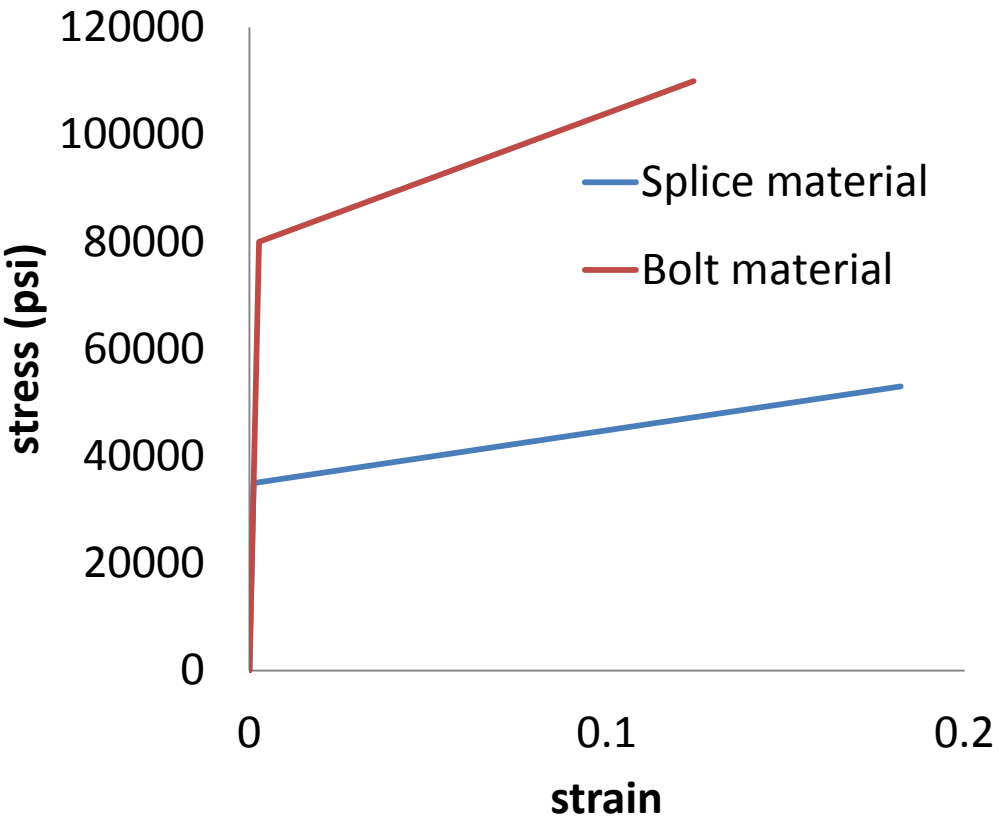

Figure 6. Engineering stress-strain curves for the splice and bolt material models.

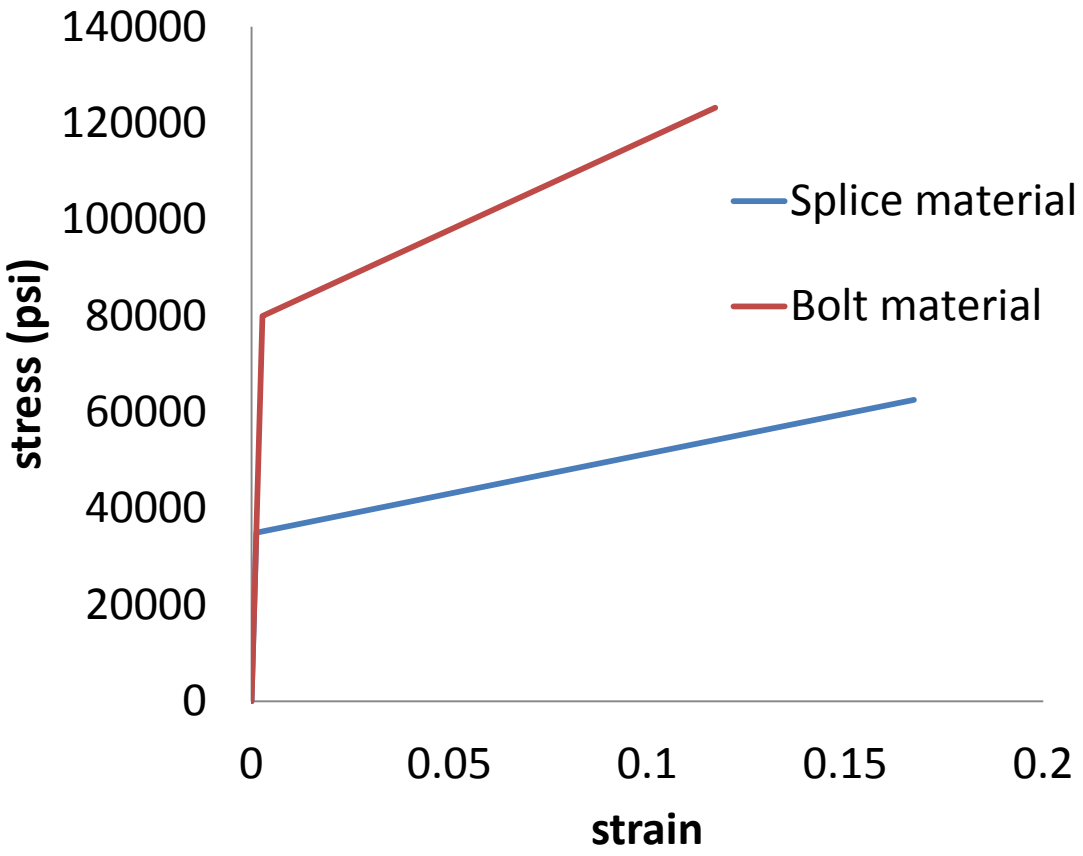

Figure 7. True stress-strain curves for the splice and bolt material models.

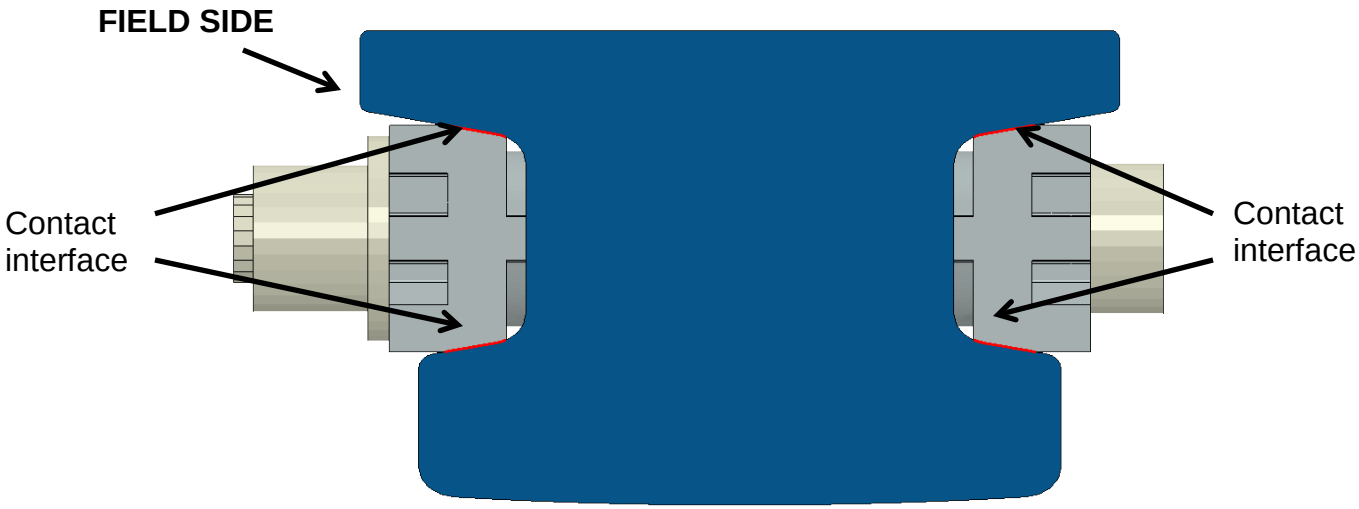

Figure 8. Interfacial condition between the splice plates and the rail.

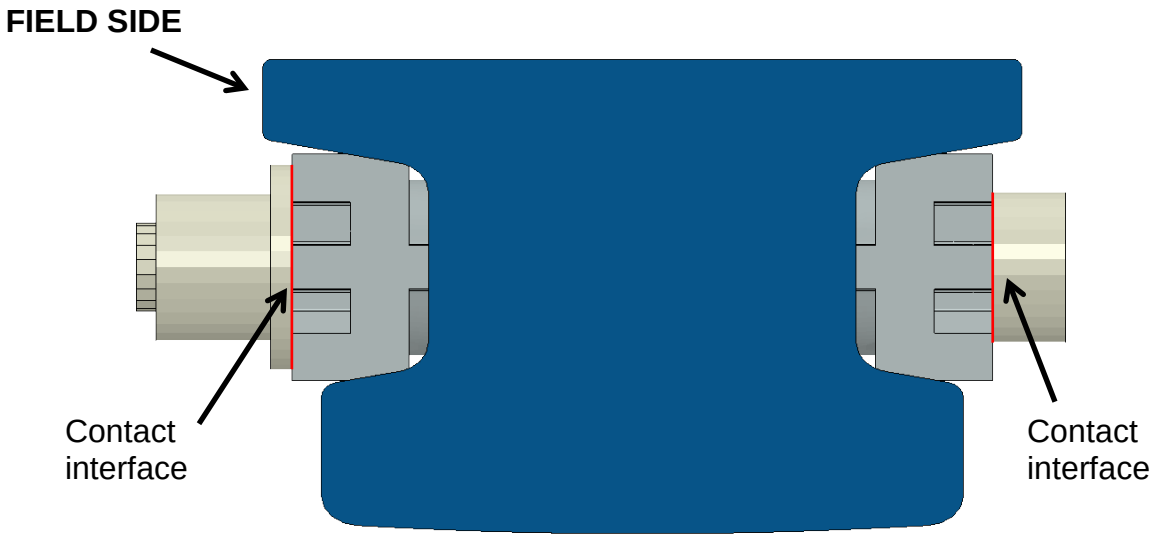

Figure 9. Interfacial condition between the splice plates and the rail.

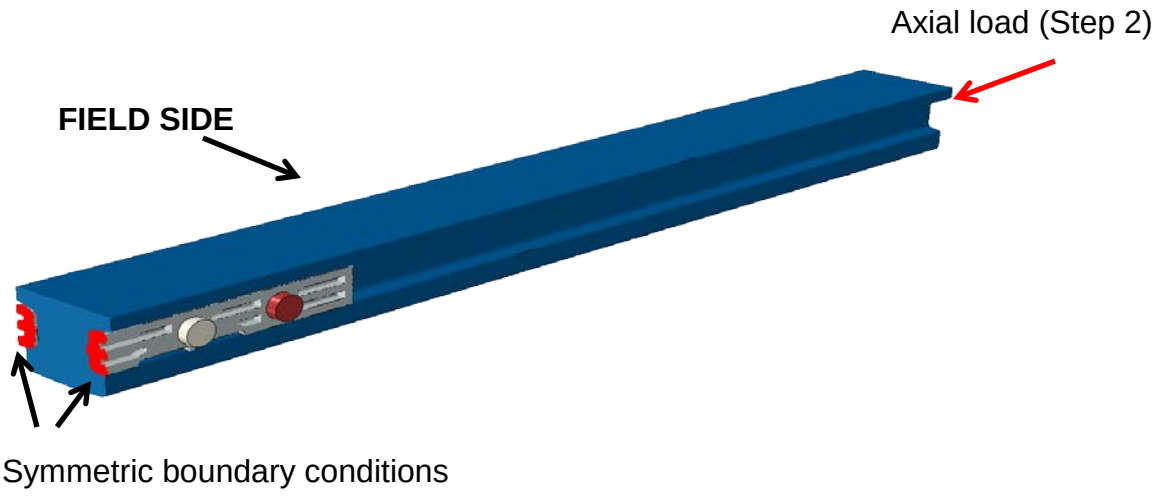

Figure 10. Prescribed loads and displacements, step 2.

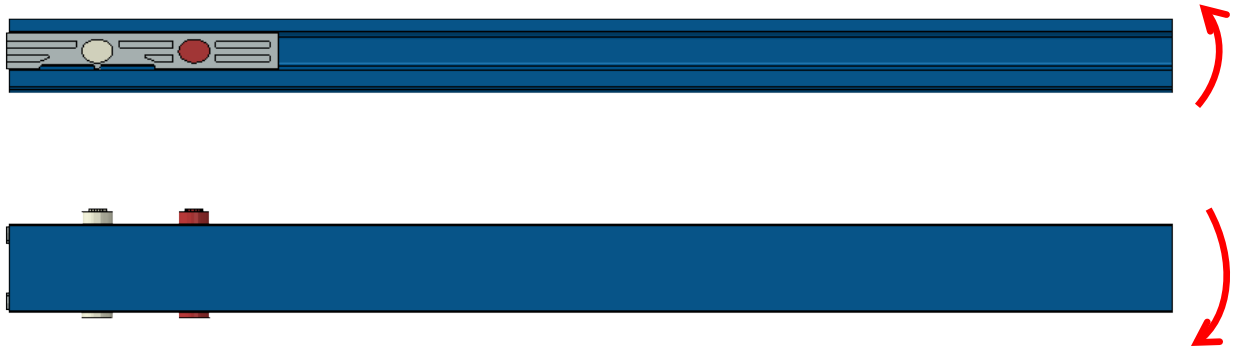

Figure 11. Prescribed loads and displacements, step 3: in-plane bending (top) and out-of-plane bending (bottom).

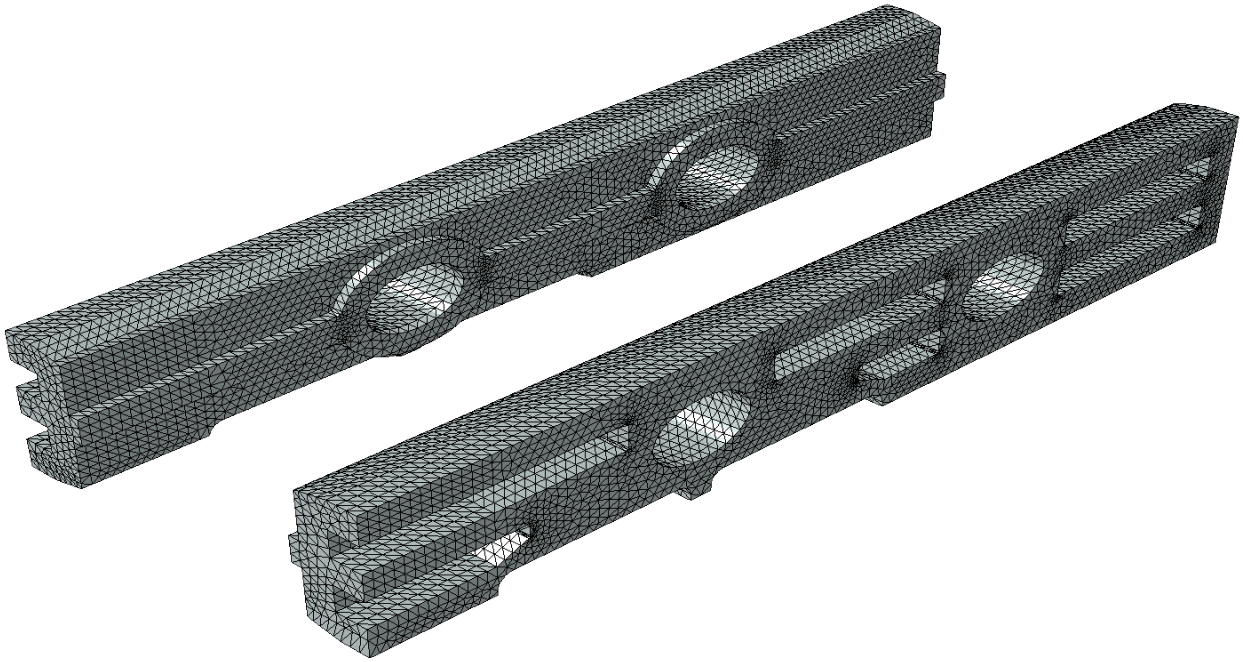

Figure 12. FE mesh of the splice plates.

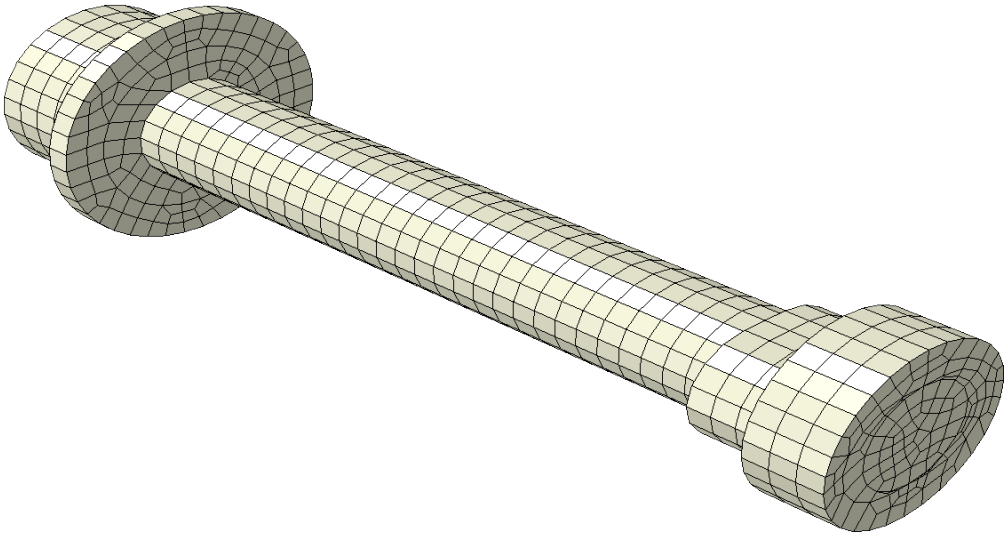

Figure 13. FE mesh of the bolt hardware.

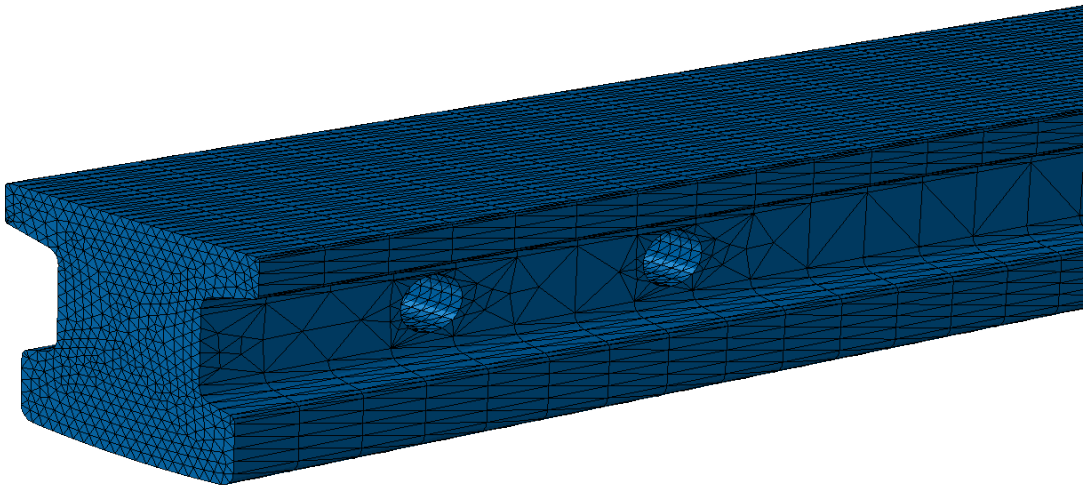

Figure 14. FE mesh of the rail.

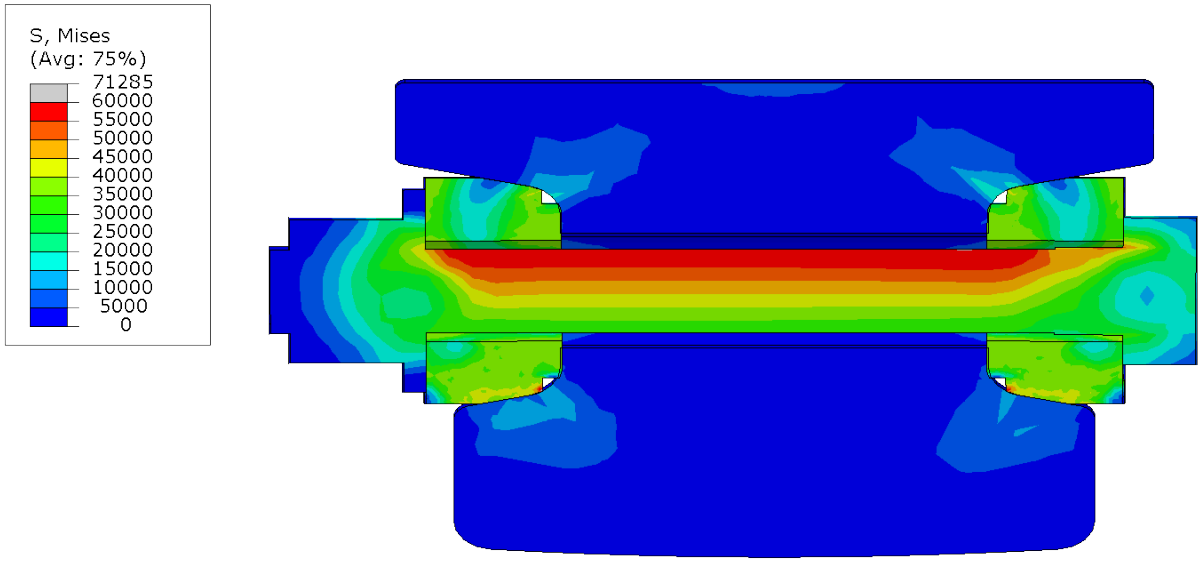

Figure 15. Mises stress distribution on the inner bolt cross section, bolt tension step.

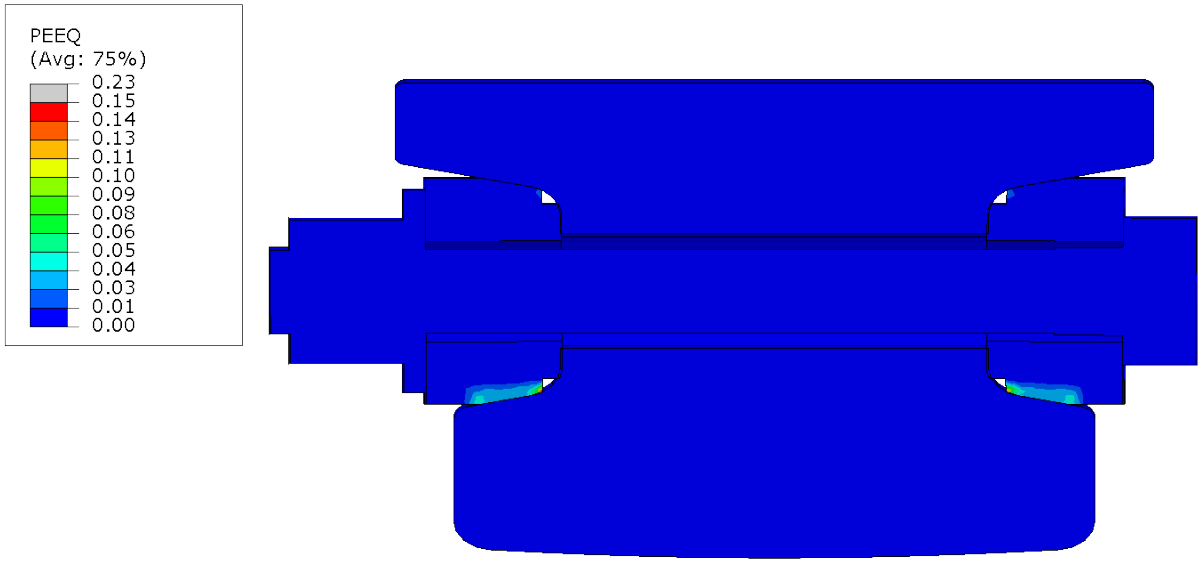

Figure 16. Effective plastic strain distribution on the inner bolt cross section, bolt tension step.

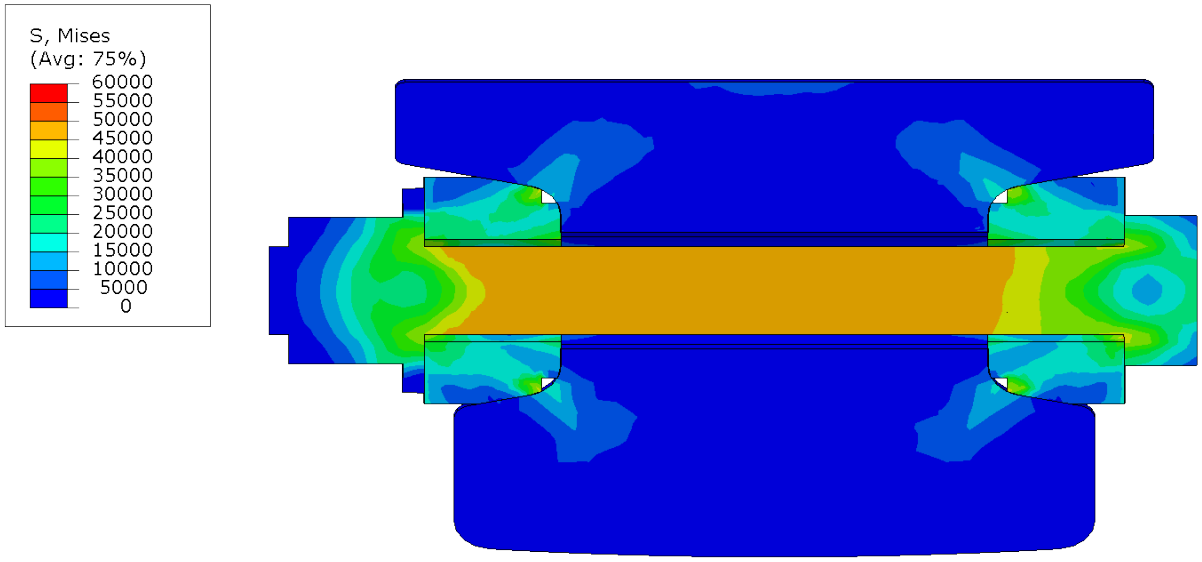

Figure 17. Mises stress distribution on the outer bolt cross section, bolt tension step.

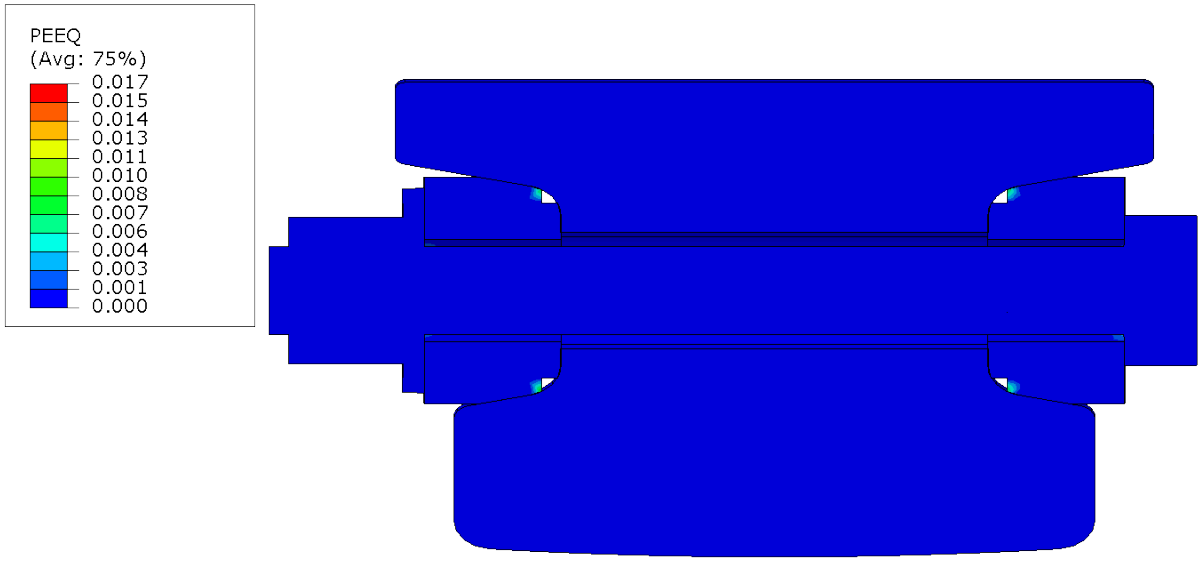

Figure 18. Effective plastic strain distribution on the outer bolt cross section, bolt tension step.

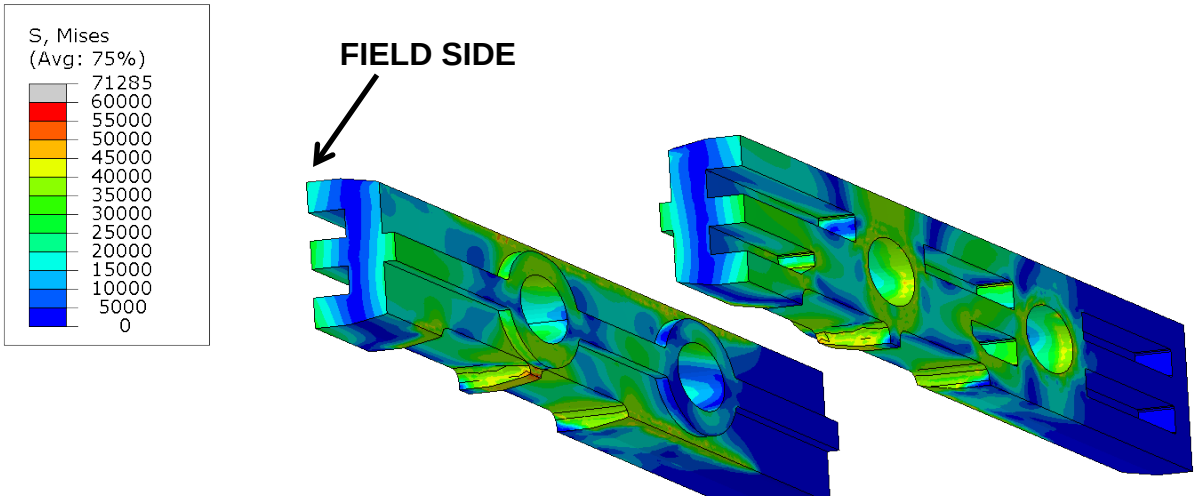

Figure 19. Mises stress distribution in the splice plates, bolt tension step.

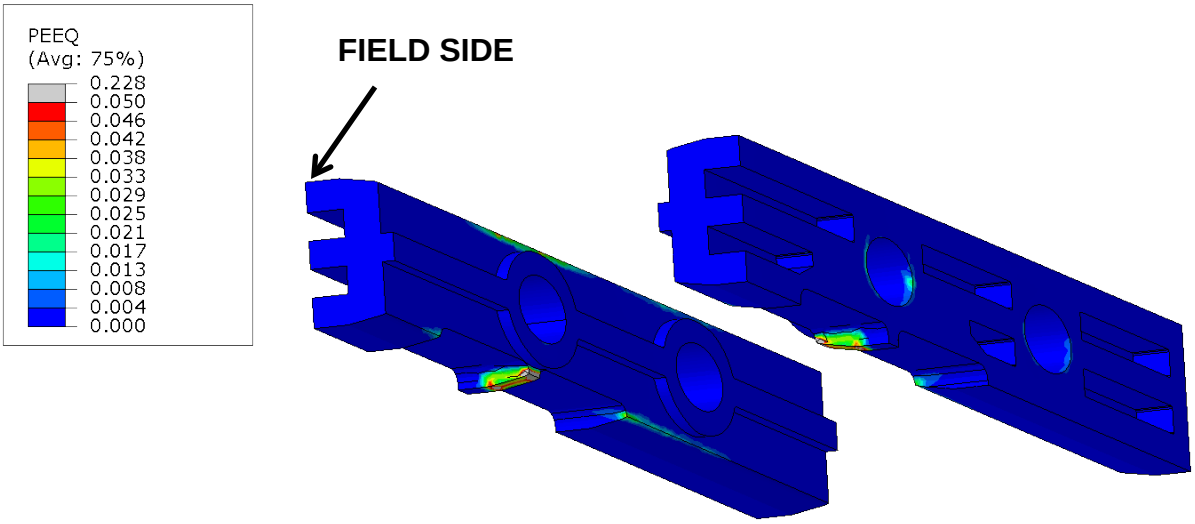

Figure 20. Effective plastic strain distribution in the splice plates, bolt tension step.

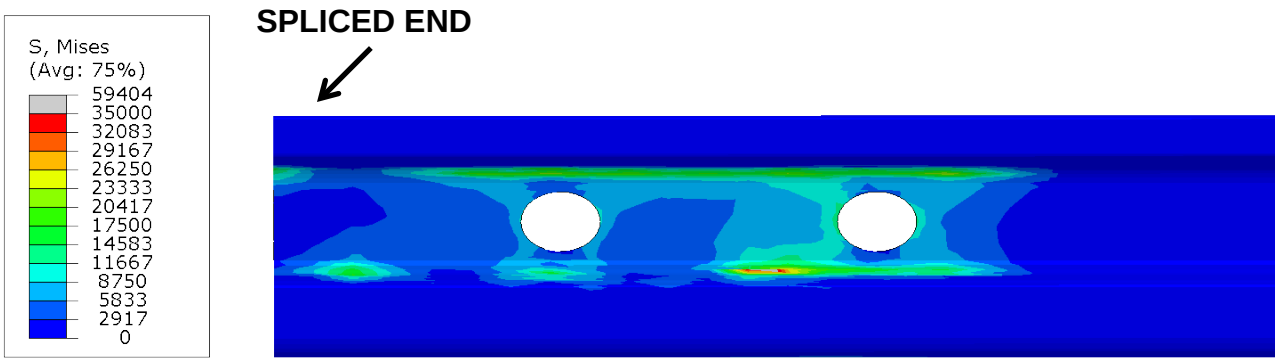

Figure 21. Mises stress distribution in the rail, assembly step.

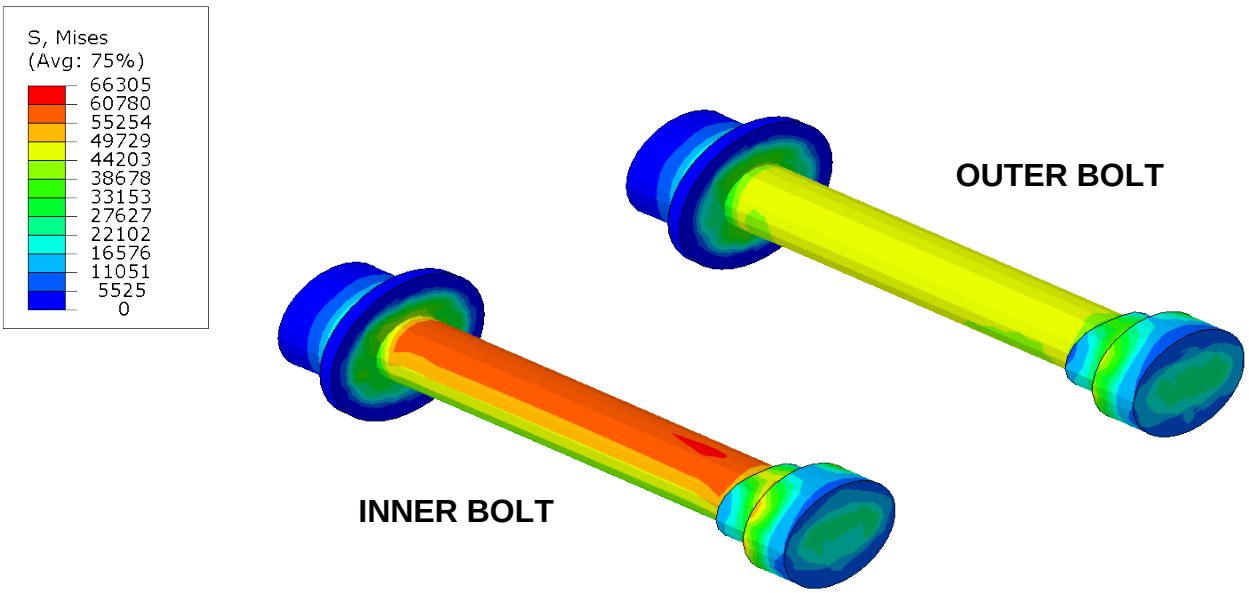

Figure 22. Mises stress distribution in the bolts, axial loading step, low axial load case.

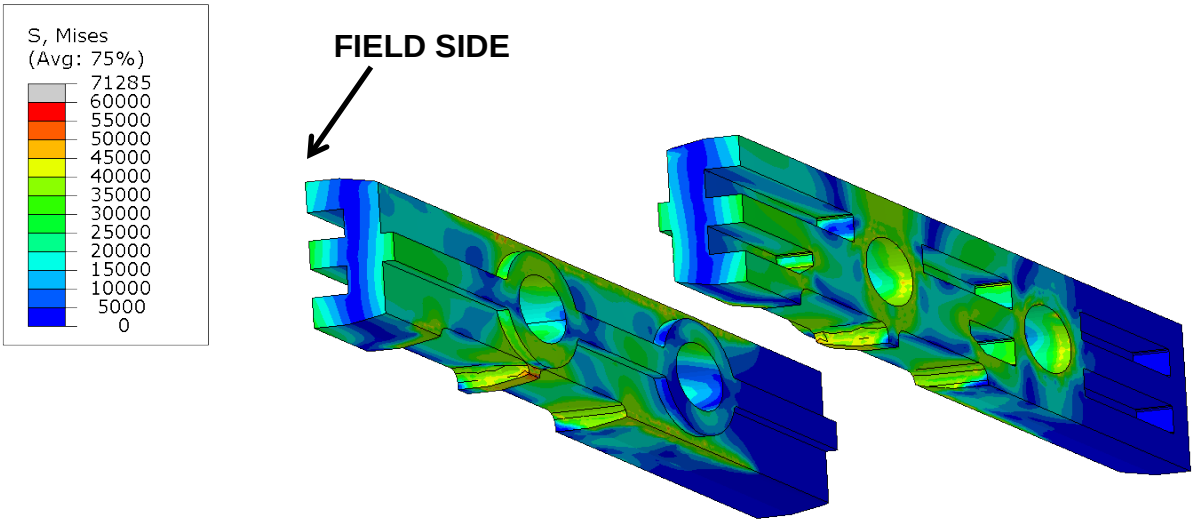

Figure 23. Mises stress distribution in the splice plates, axial loading step, low axial load case.

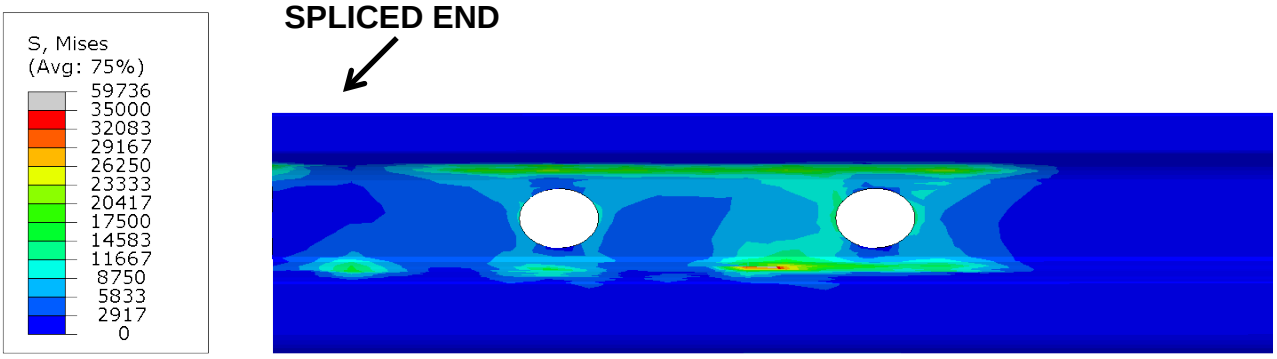

Figure 24. Mises stress distribution in the rail, axial loading step, low axial load case.

Figure 25. Deformed shape of the structure with deformation magnified 10 times and undeformed shape superposed, axial loading step, high axial load case.

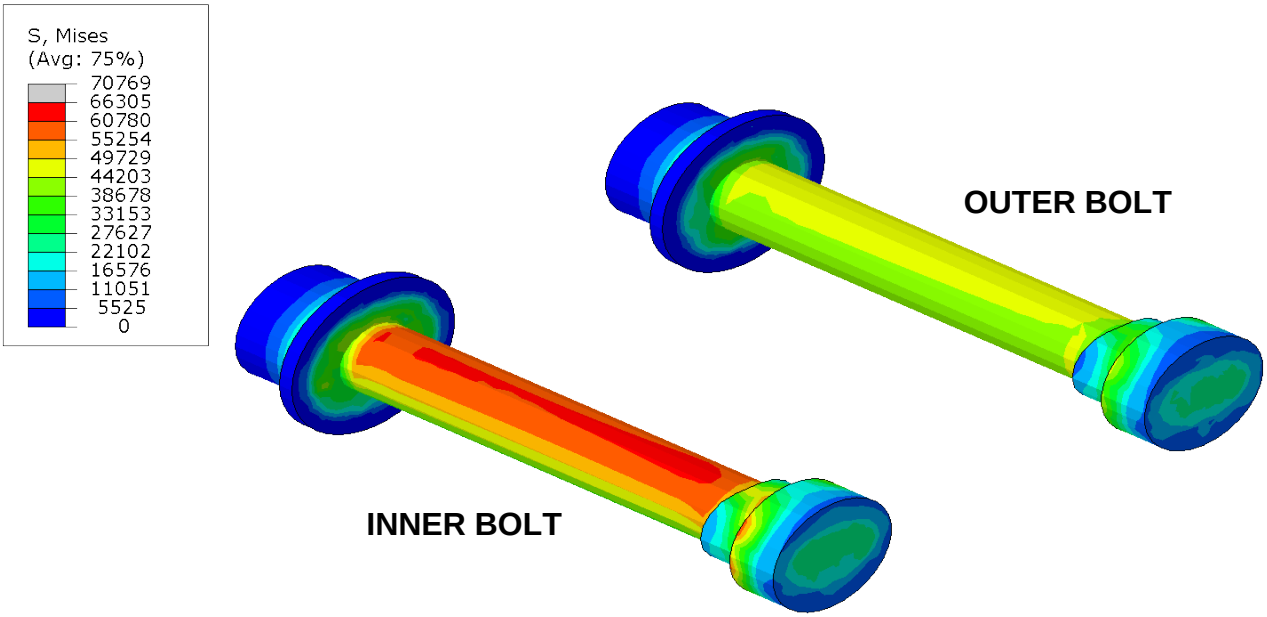

Figure 26. Mises stress distribution in the bolts, axial loading step, high axial load case.

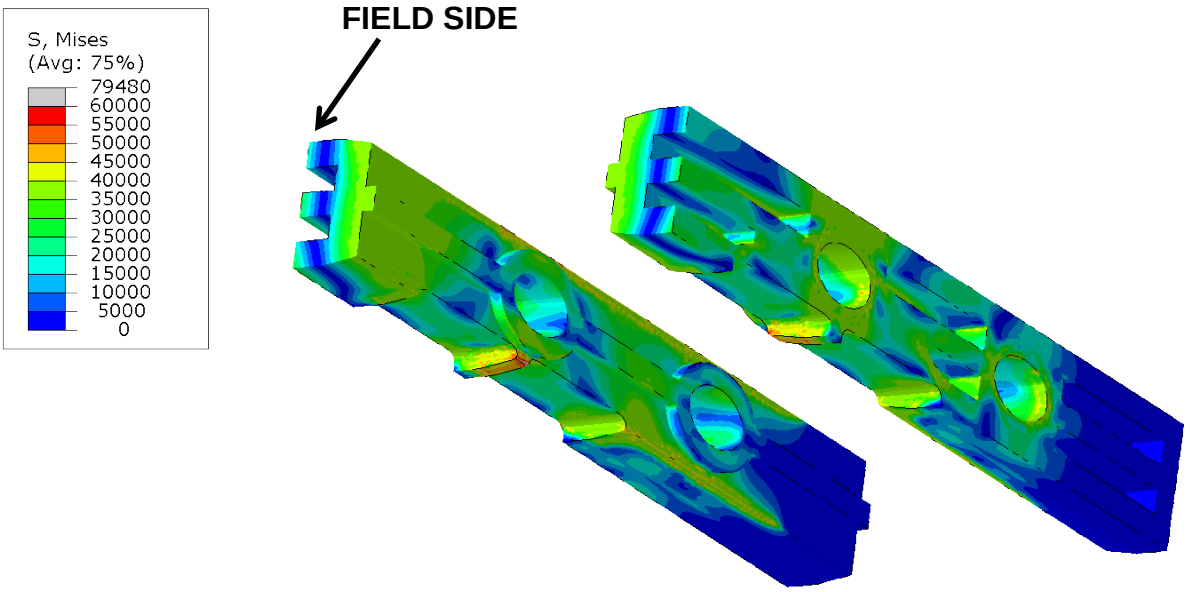

Figure 27. Mises stress distribution in the splice plates, axial loading step, high axial load case.

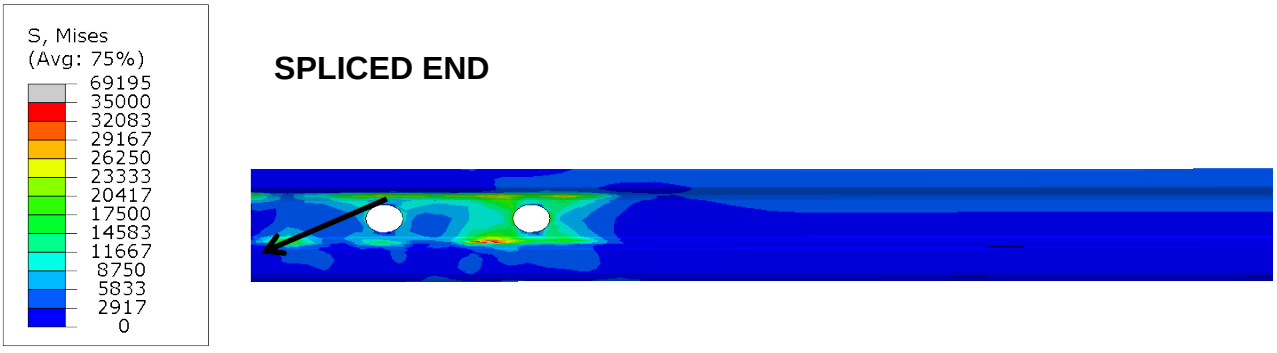

Figure 28. Mises stress distribution in the rail, axial loading step, high axial load case.

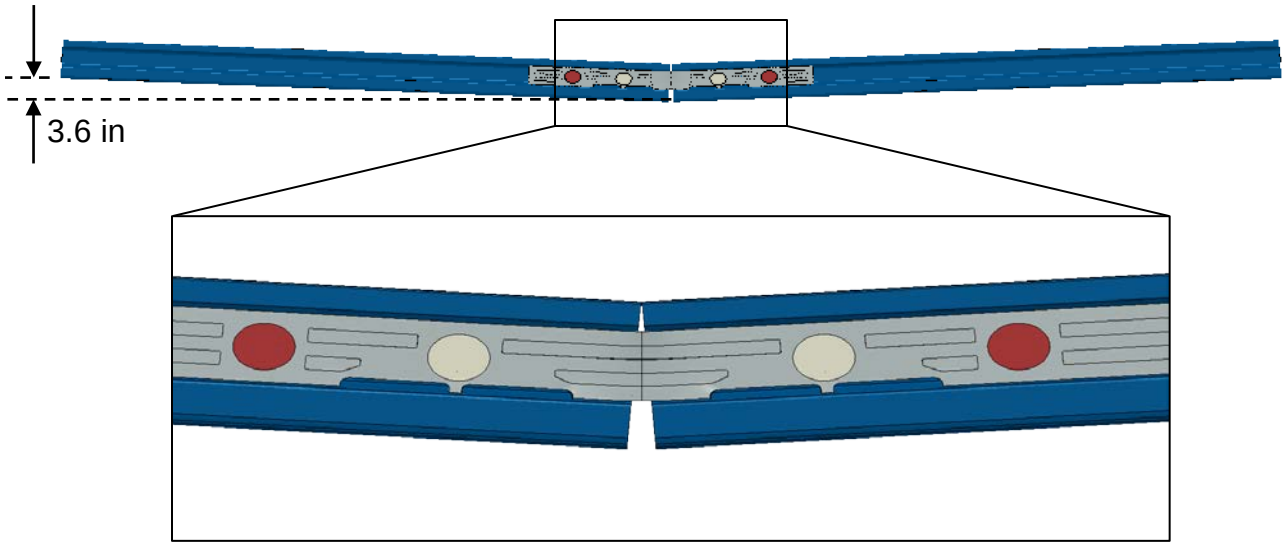

Figure 29. Deformed shape of the structure with the symmetric half also shown, in-plane bending step.

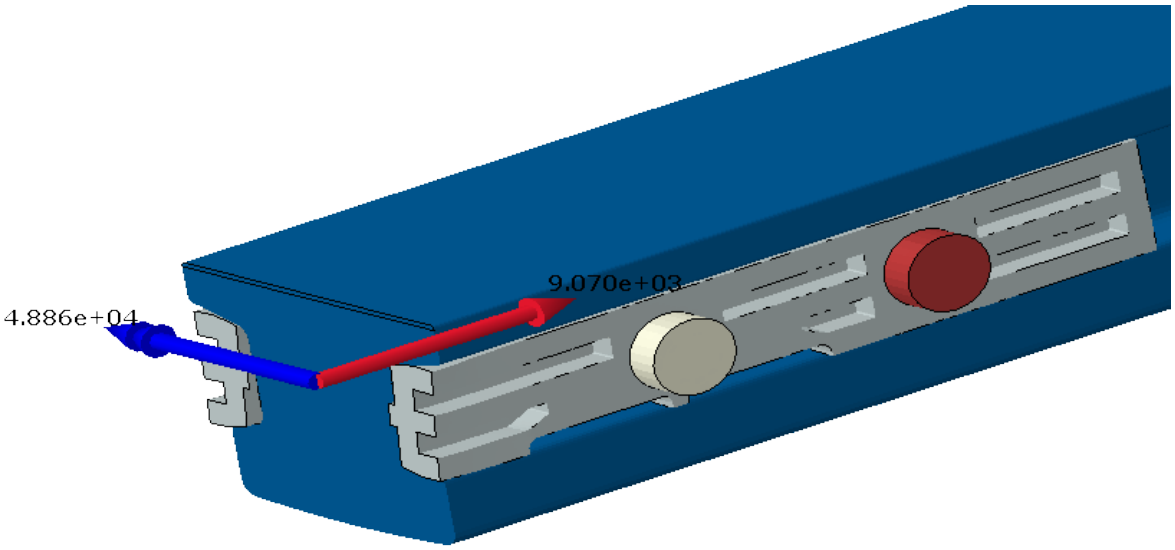

Figure 30. FBD of the structure, in-plane bending step, low axial load case.

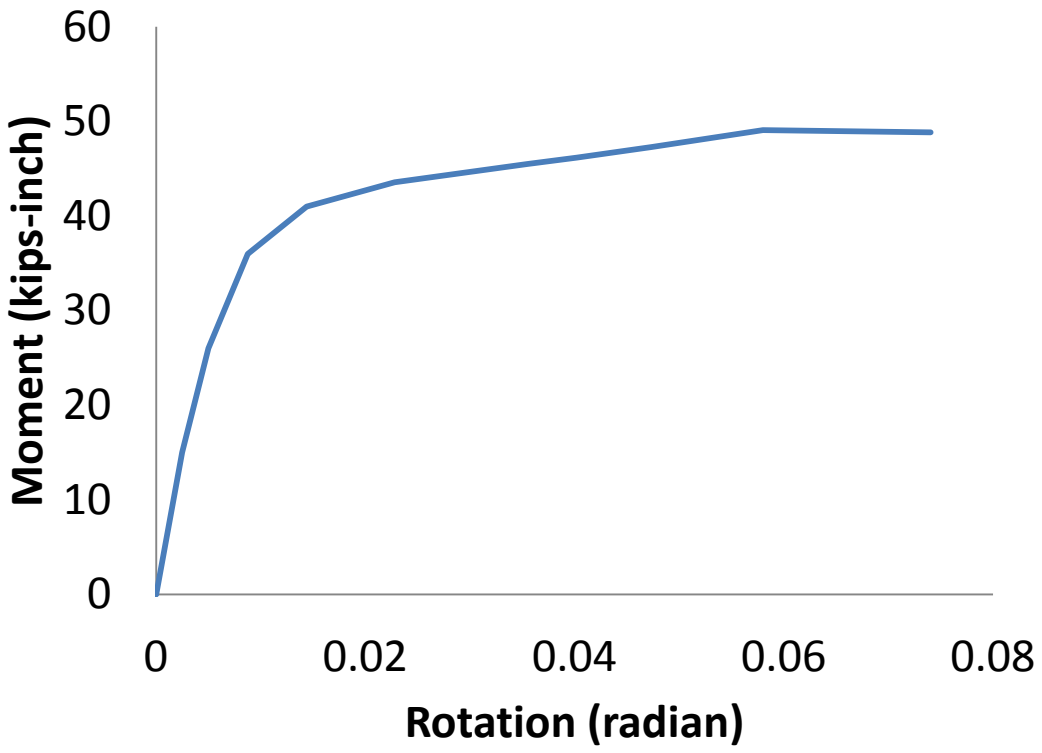

Figure 31. Moment vs. applied rotation curve, in-plane bending step, low axial loading case.

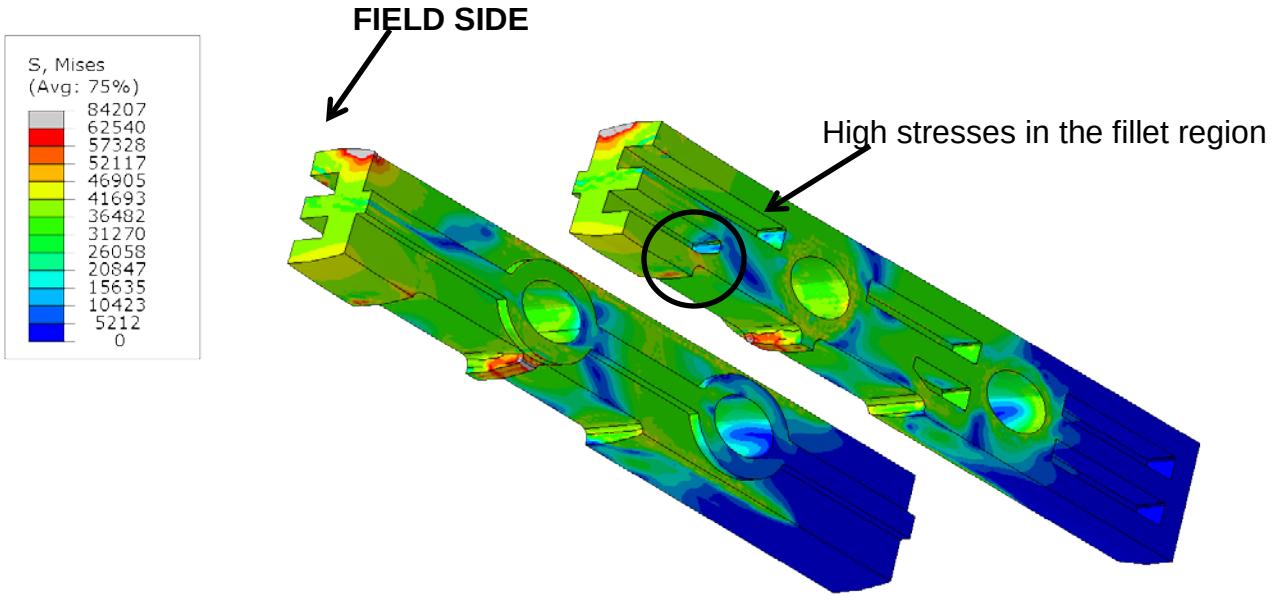

Figure 32. Mises stress distribution in the splice plates, in-plane bending step, low axial load case.

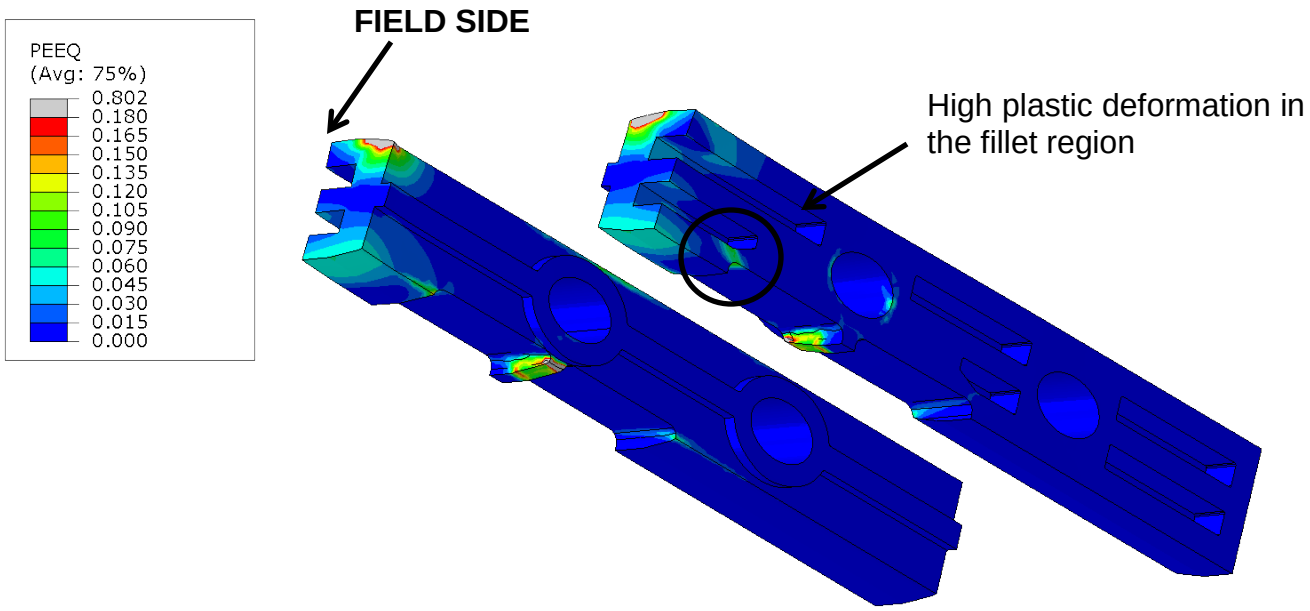

Figure 33. Effective plastic strain distribution in the splice plates, in-plane bending step, low axial load case.

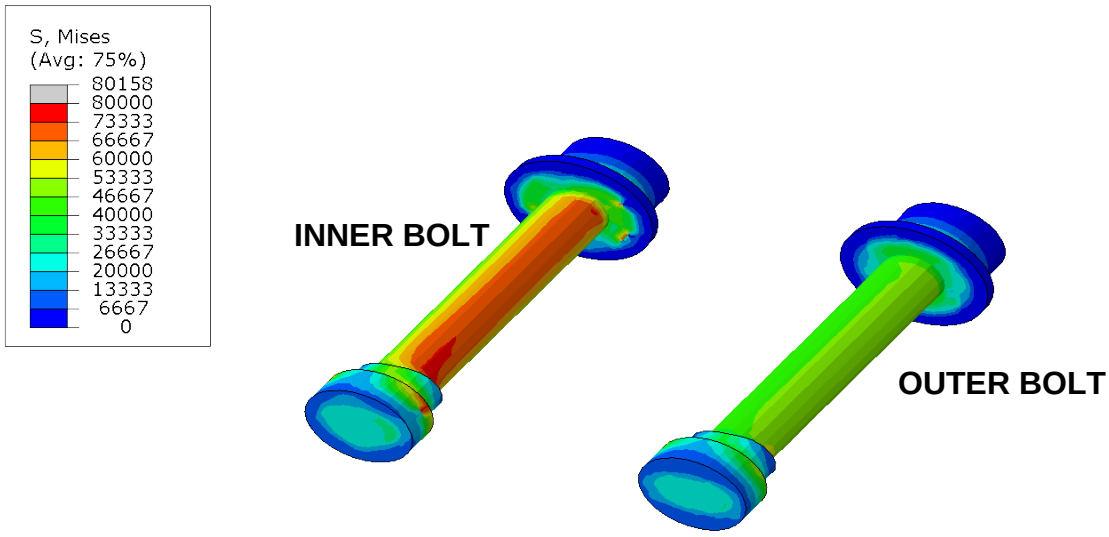

Figure 34. Mises stress distribution in the bolts, in-plane bending step, low axial load case.

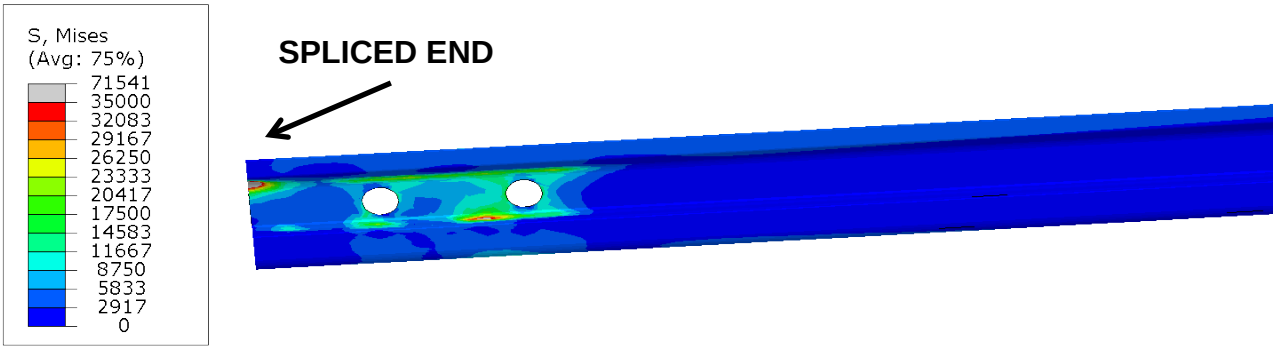

Figure 35. Mises stress distribution in the rail, in-plane bending step, low axial load case.

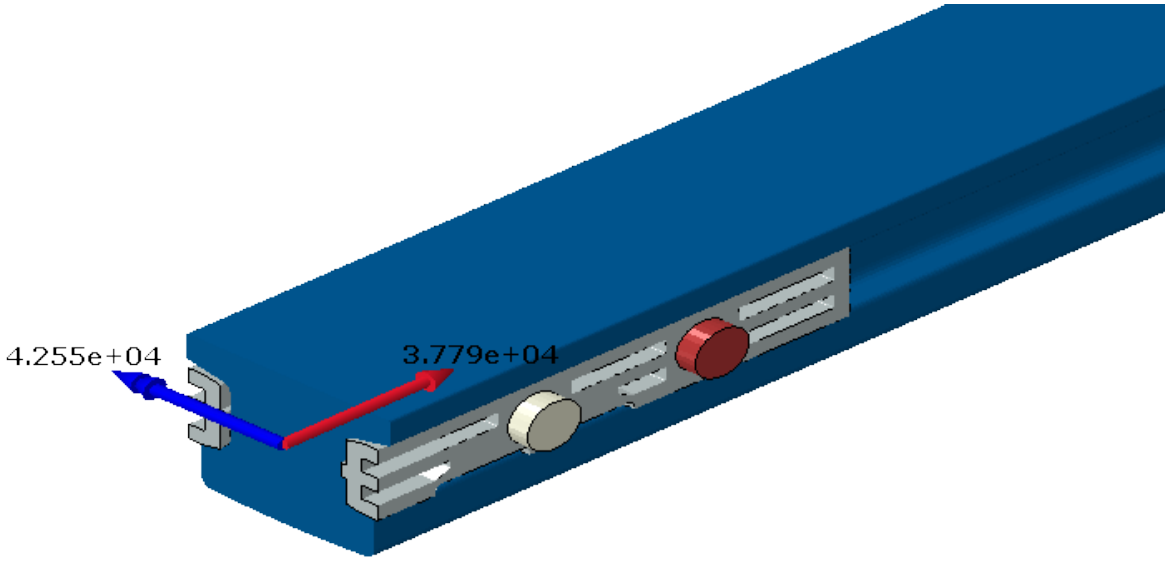

Figure 36. FBD of the structure, in-plane bending step, high axial load case.

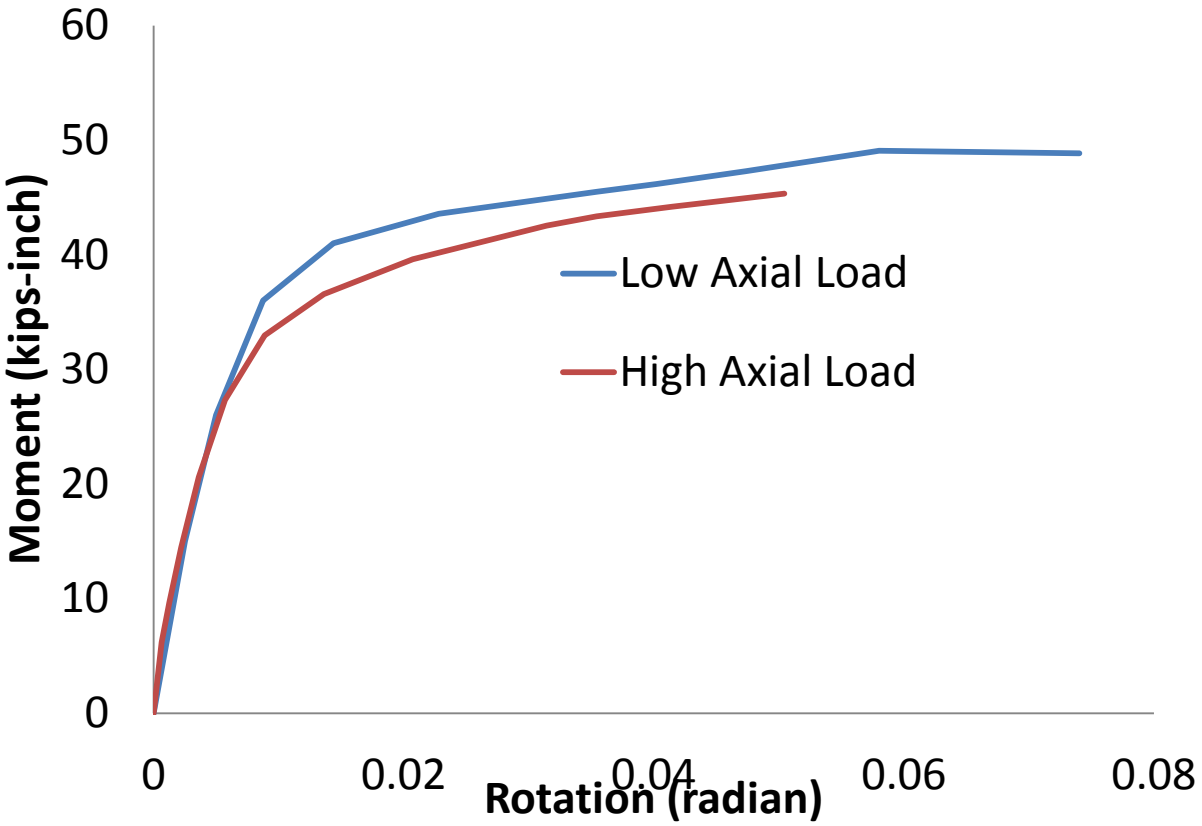

Figure 37. Moment vs. applied rotation curve, in-plane bending step, both axial loading cases.

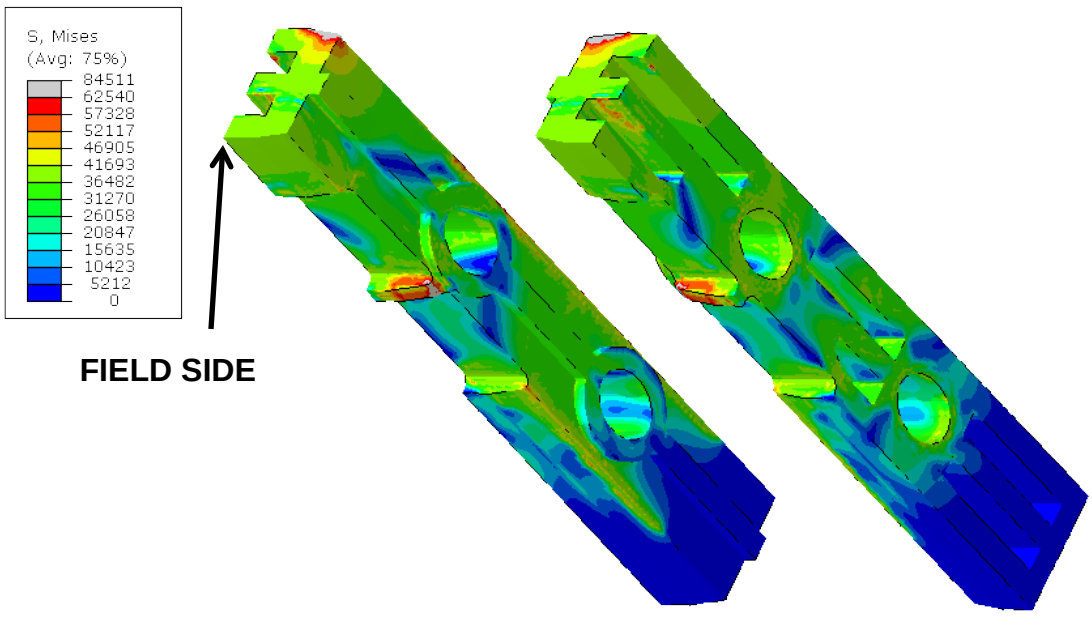

Figure 38. Mises stress distribution in the splice plates, in-plane bending step, high axial load case.

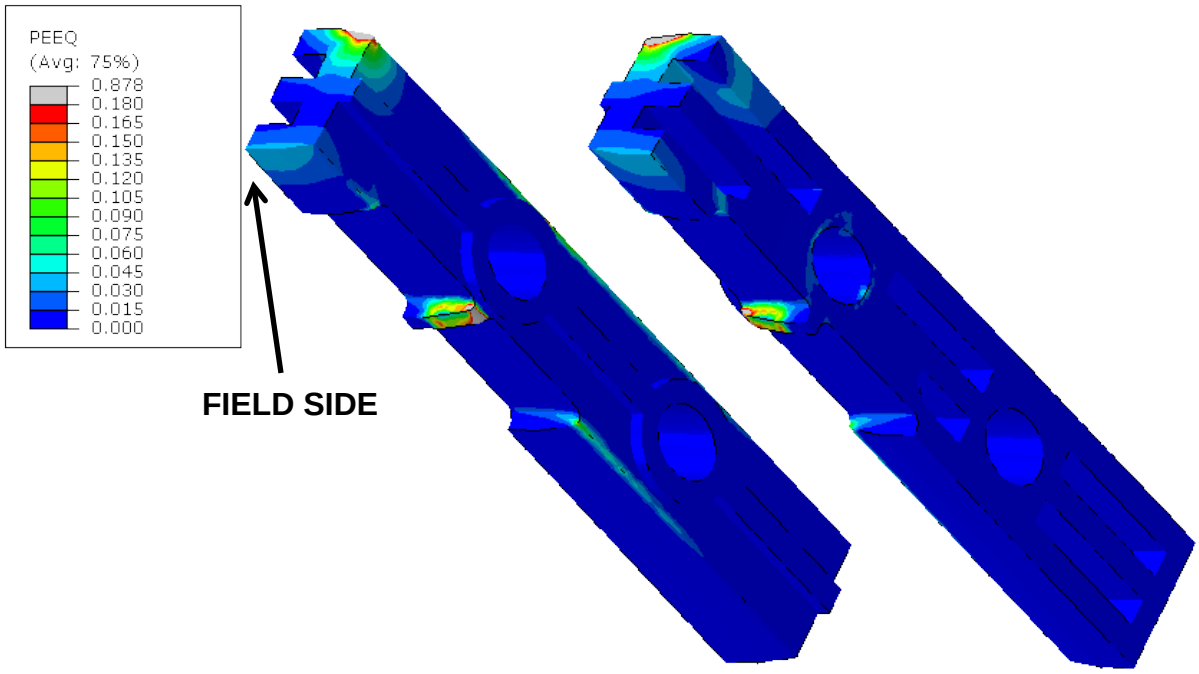

Figure 39. Effective plastic strain distribution in the splice plates, in-plane bending step, high axial load case.

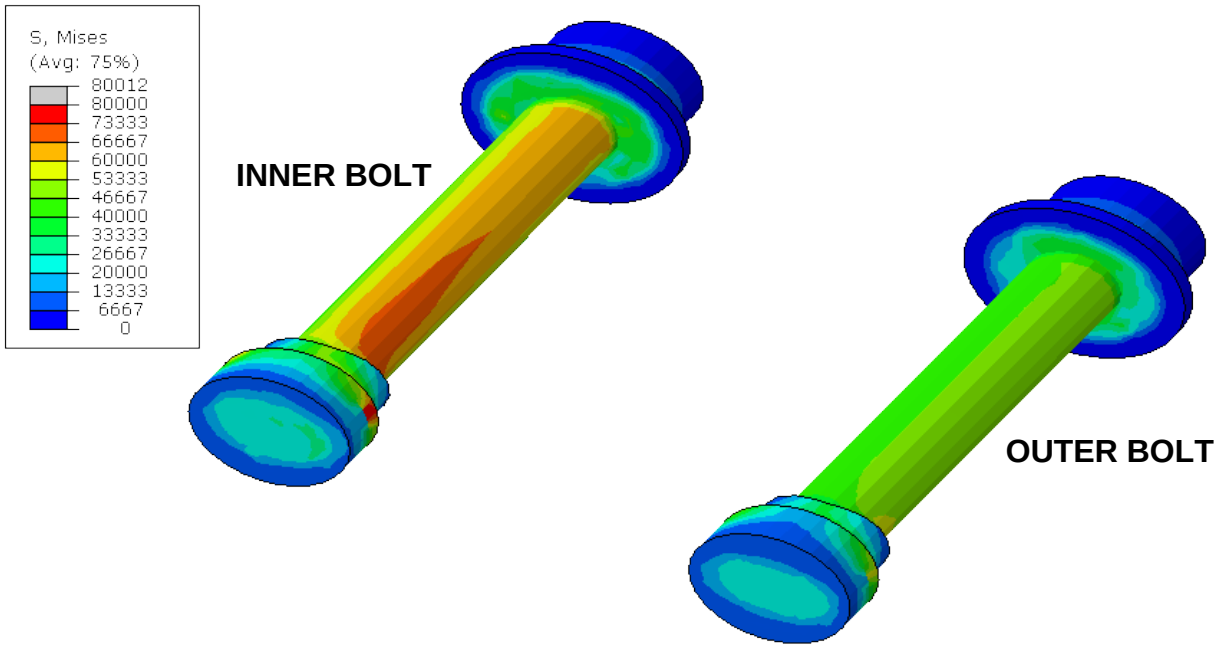

Figure 40. Mises stress distribution in the bolts, in-plane bending step, high axial load case.

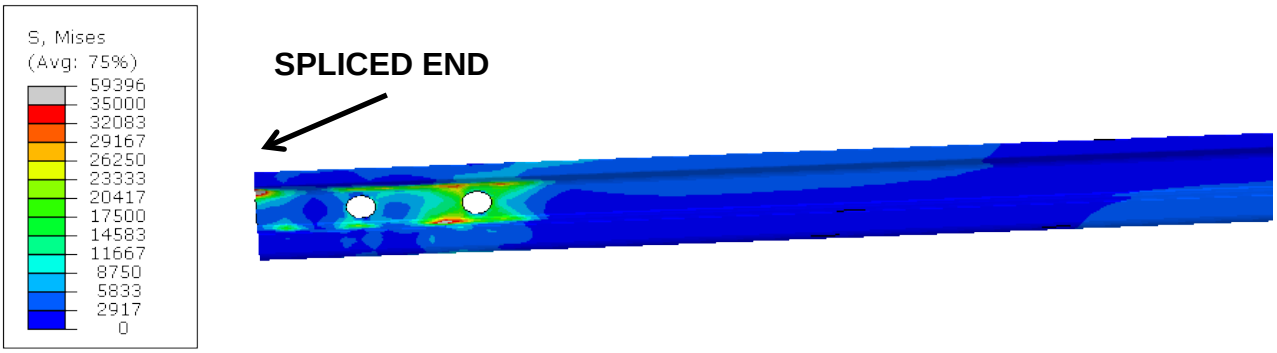

Figure 41. Mises stress distribution in the rail, in-plane bending step, high axial load case.

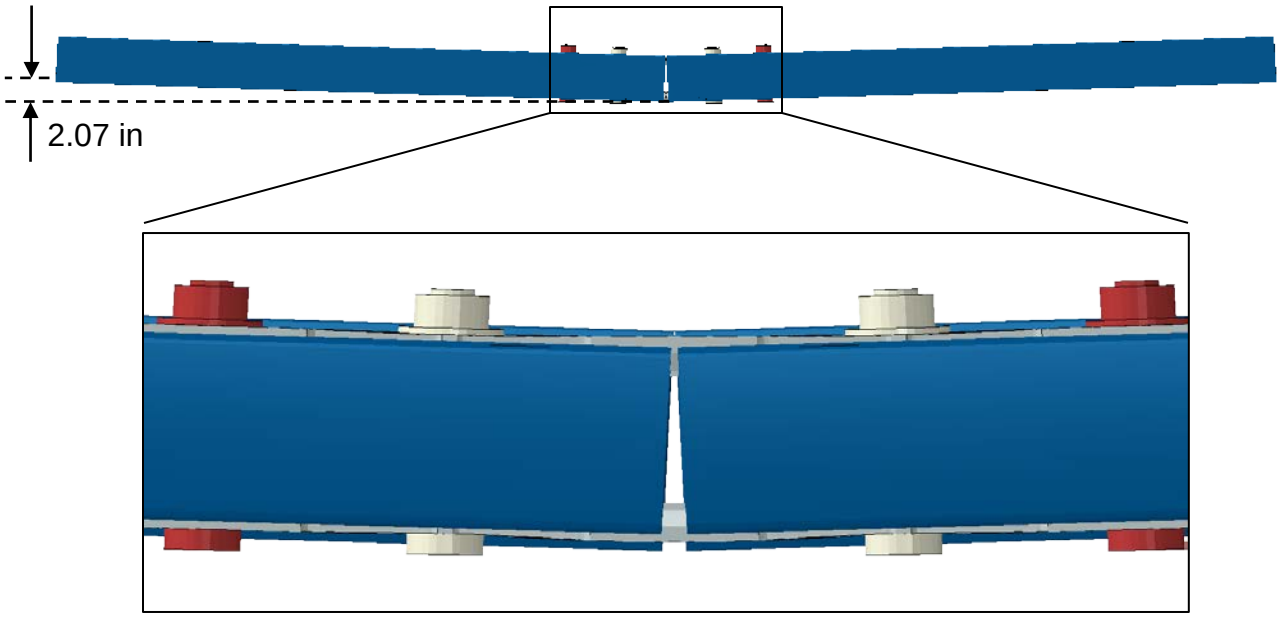

Figure 42. Deformed shape of the structure with the symmetric half shown, out-of-plane bending step.

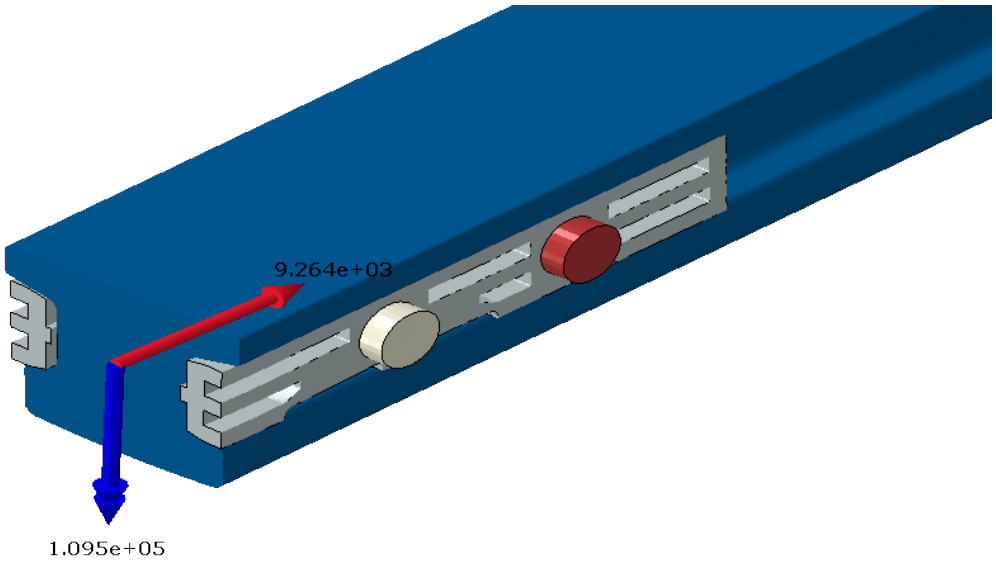

Figure 43. FBD of the structure, out-of-plane bending step, low axial load case.

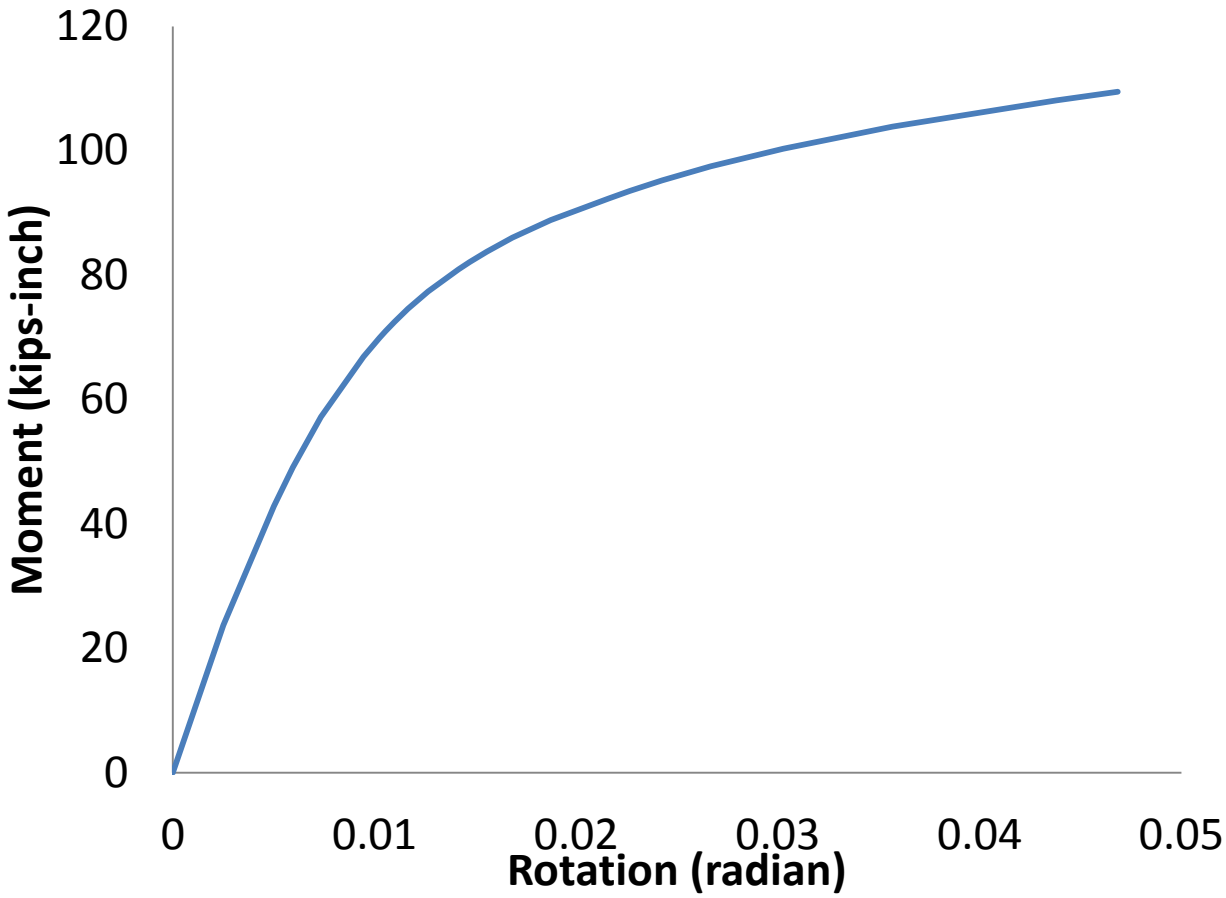

Figure 44. Moment vs. applied rotation curve, out-of-plane bending step, low axial load case.

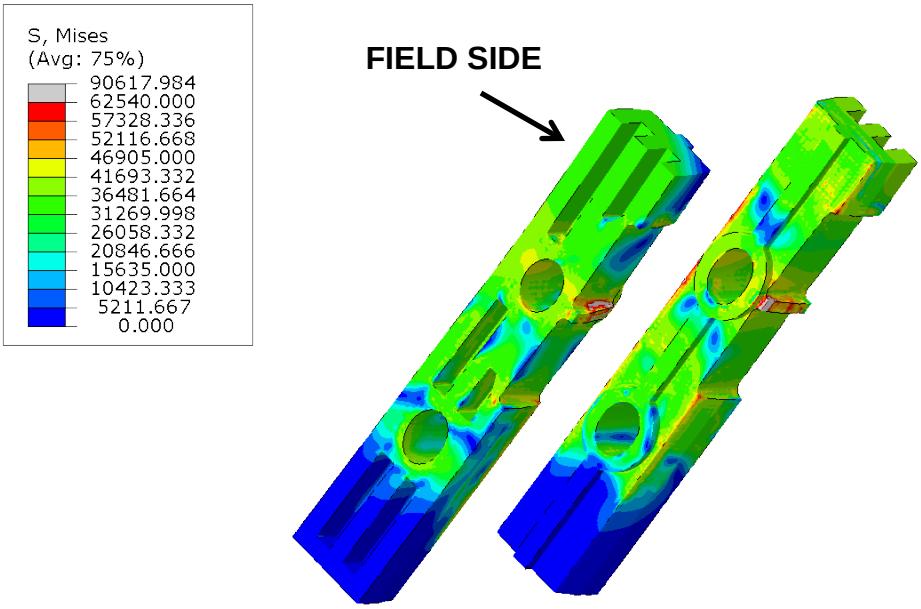

Figure 45. Mises stress distribution in the splice plates, out-of-plane bending step, low axial load case.

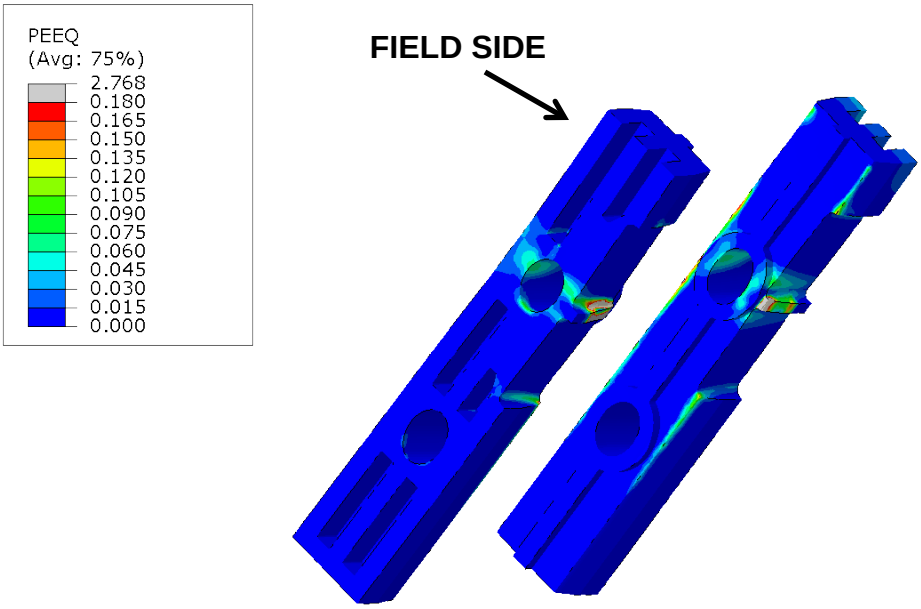

Figure 46. Effective plastic strain distribution in the splice plates, out-of-plane bending step, low axial load case.

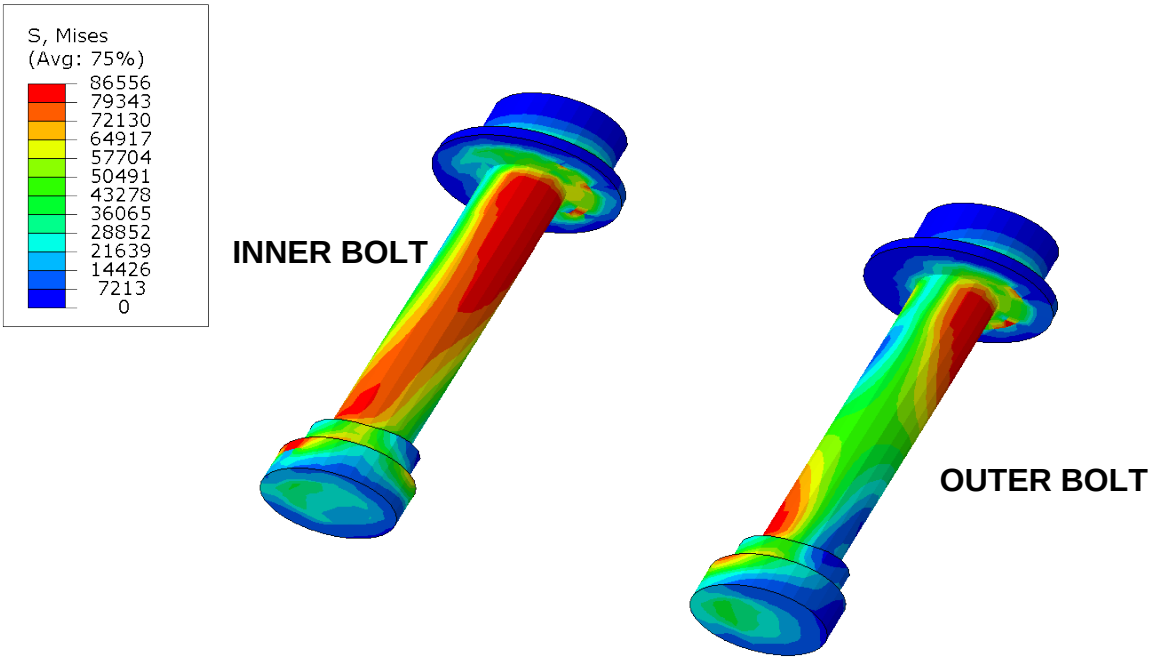

Figure 47. Mises stress distribution in the bolts, out-of-plane bending step, low axial load case.

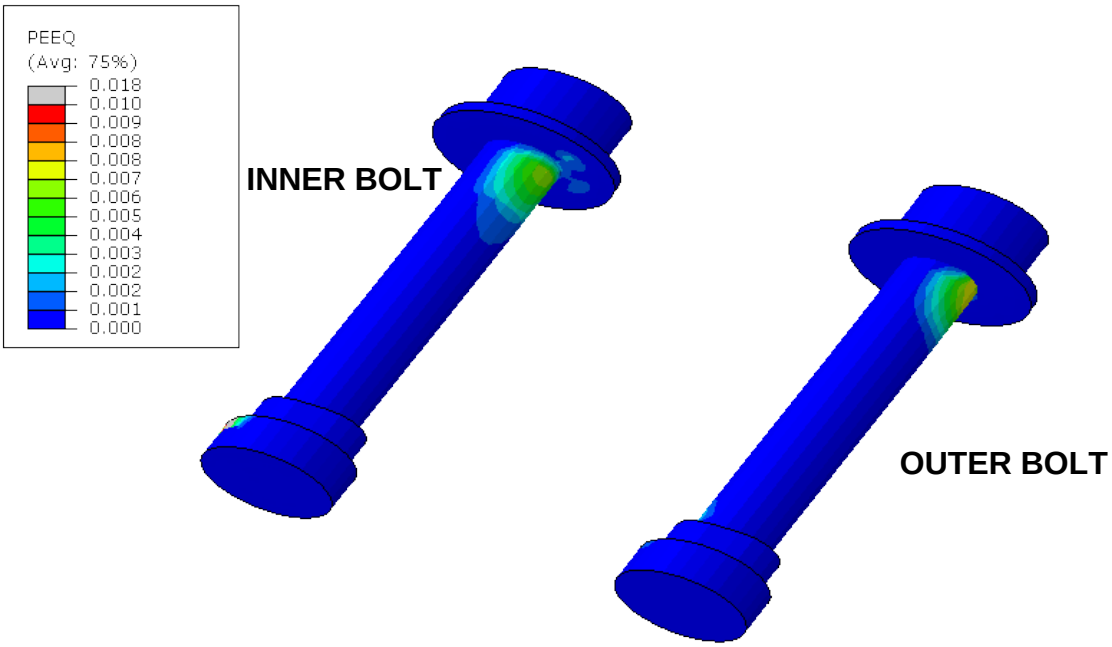

Figure 48. Effective plastic strain distribution in the bolts, out-of-plane bending step, low axial load case.

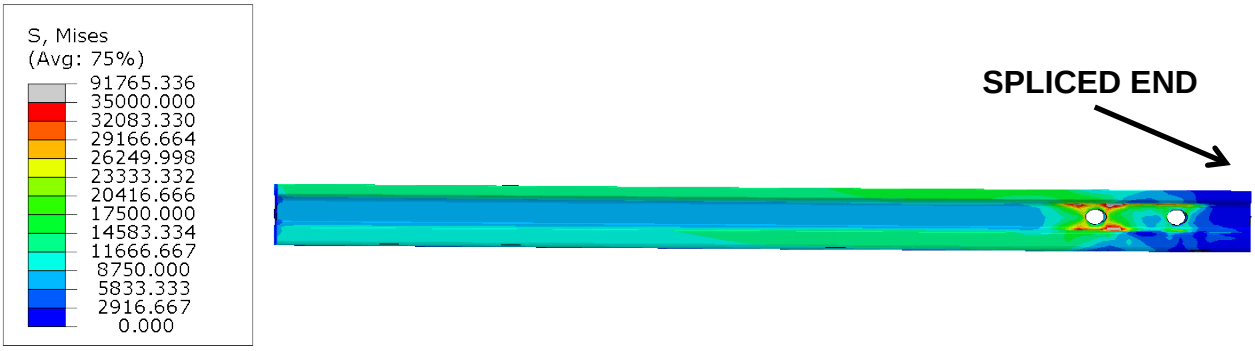

Figure 49. Mises stress distribution in the rail, out-of-plane bending step, low axial load case.

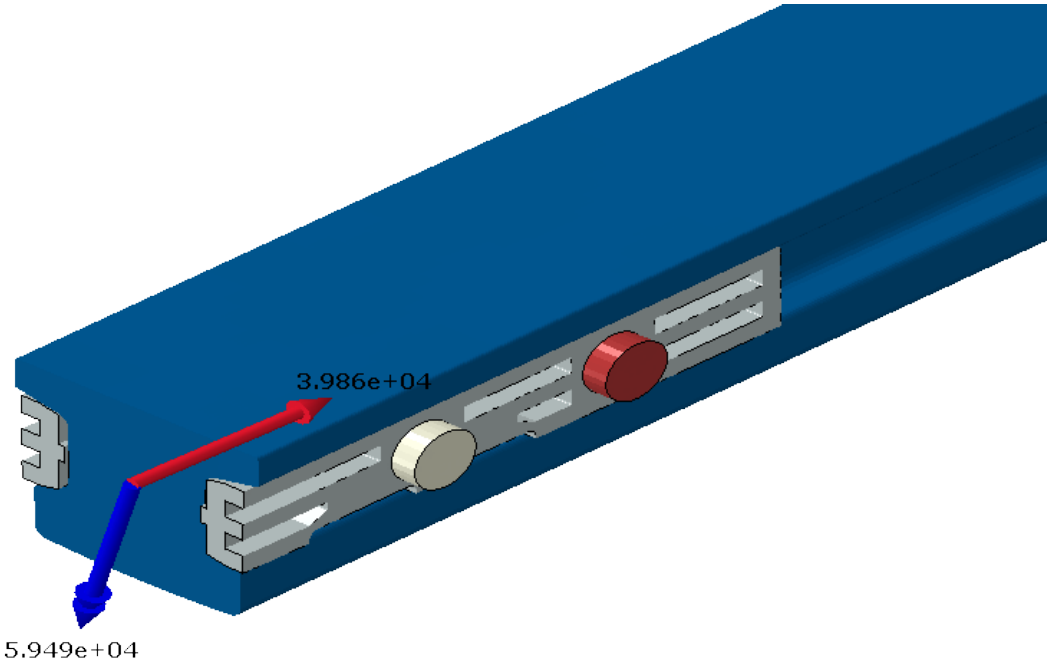

Figure 50. FBD of the structure, out-of-plane bending step, high axial load case.

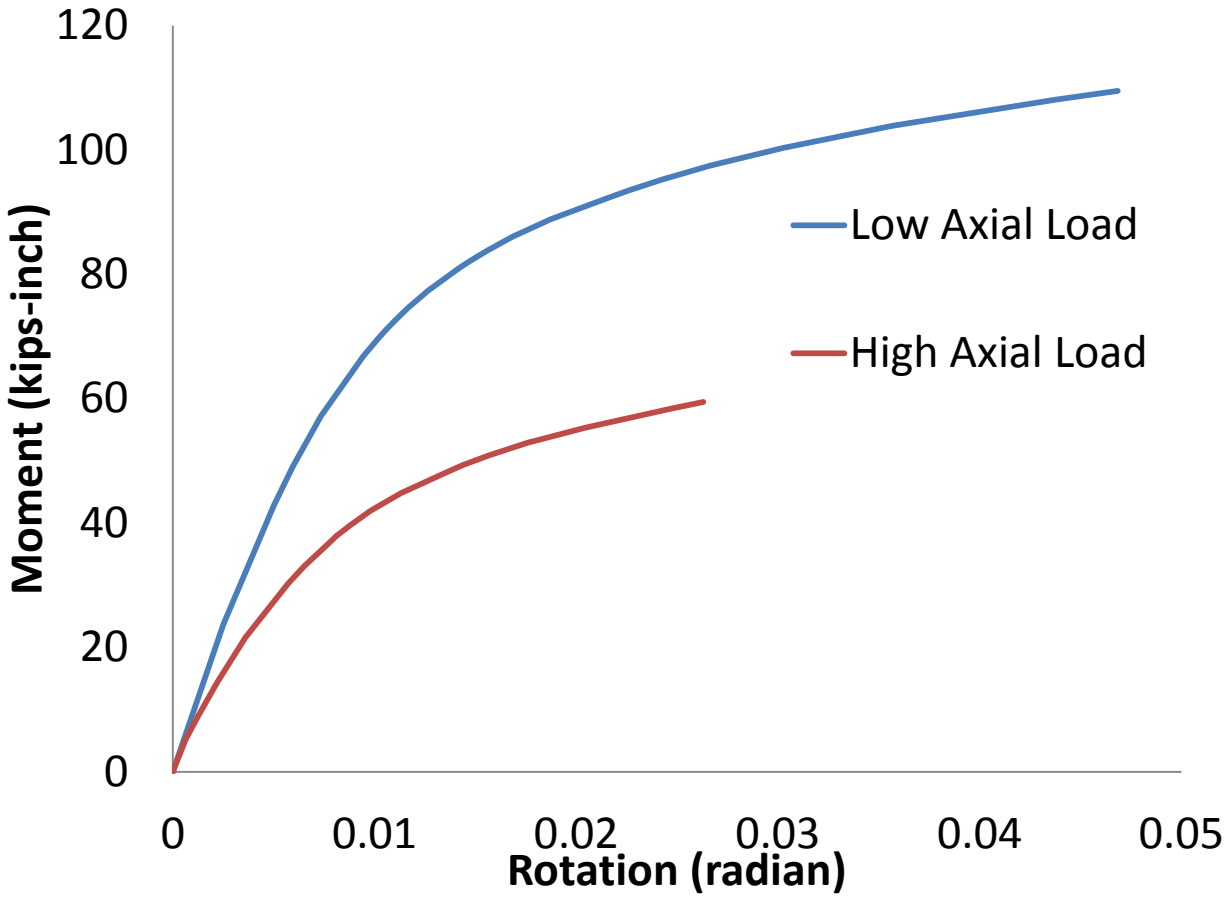

Figure 51. Moment vs. applied rotation curve, out-of-plane bending step, both axial loading cases.

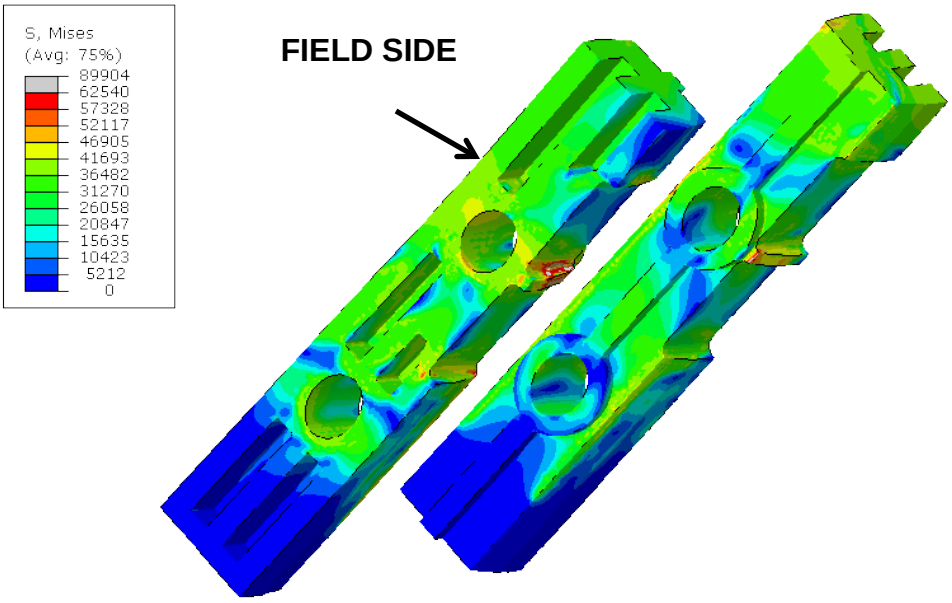

Figure 52. Mises stress distribution in the splice plates, out-of-plane bending step, high axial load case.

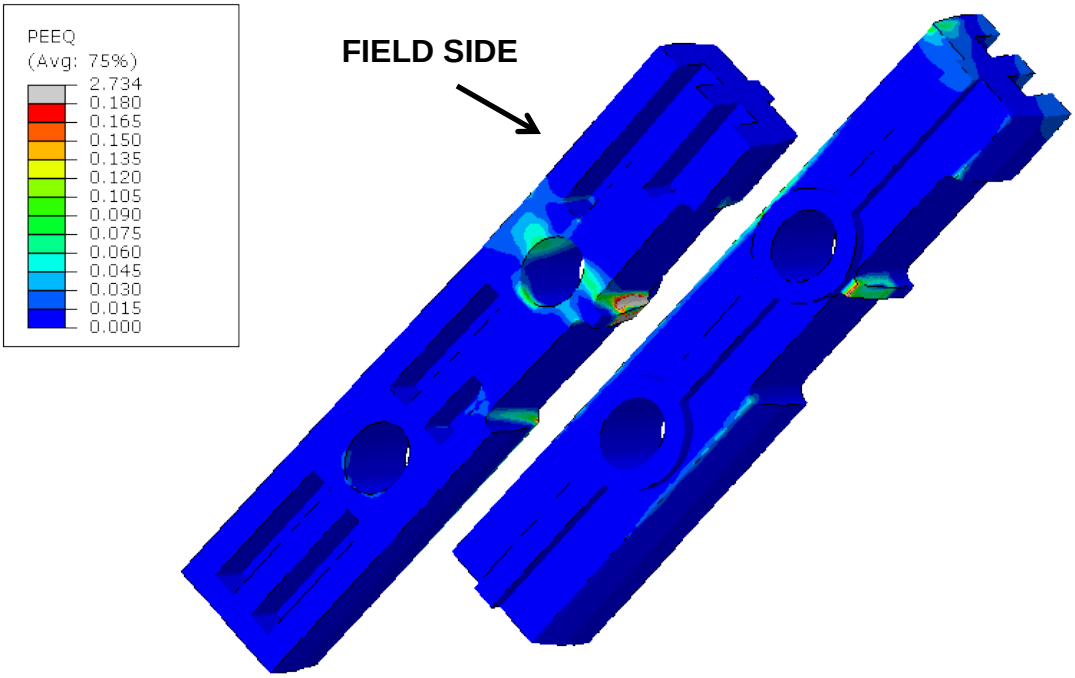

Figure 53. Effective plastic strain distribution in the splice plates, out-of-plane bending step, high axial load case.

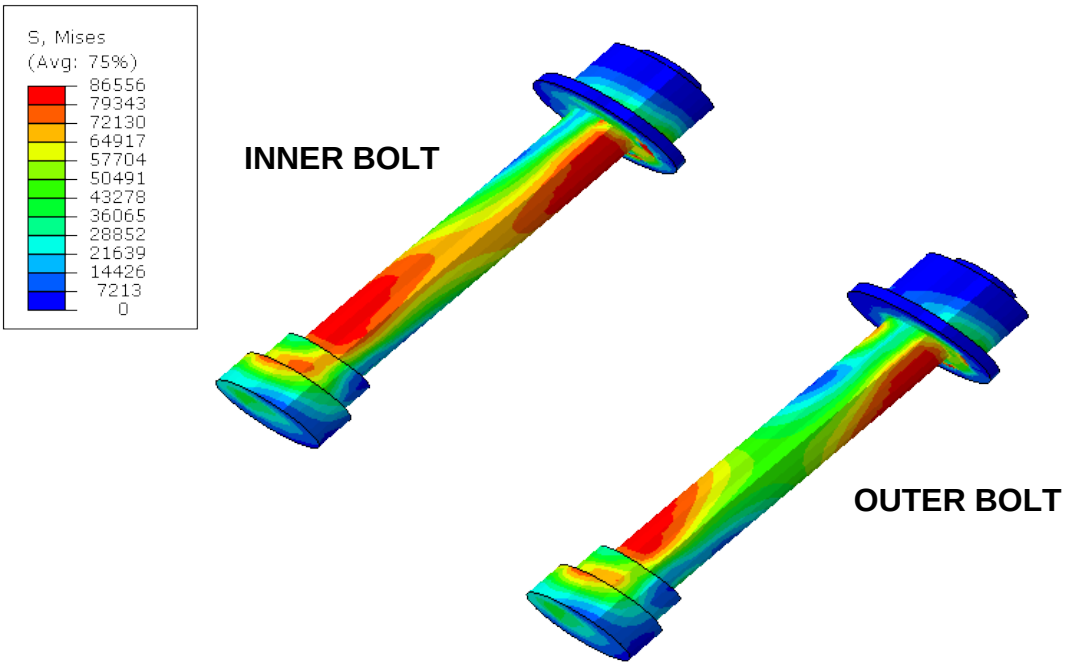

Figure 54. Mises stress distribution in the bolts, out-of-plane bending step, high axial load case.

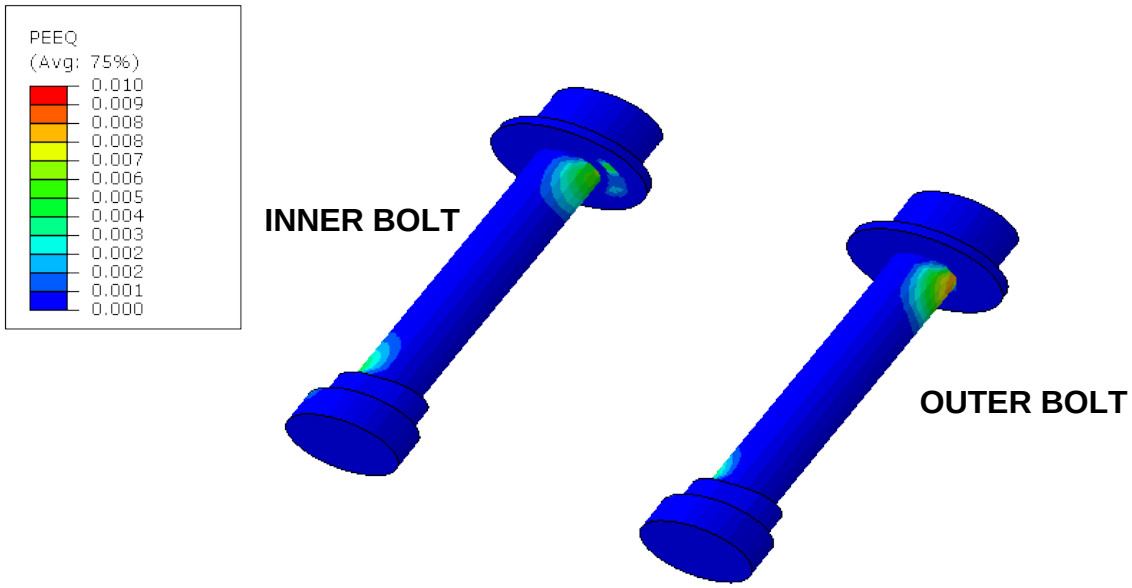

Figure 55. Effective plastic strain distribution in the bolts, out-of-plane bending step, high axial load case.

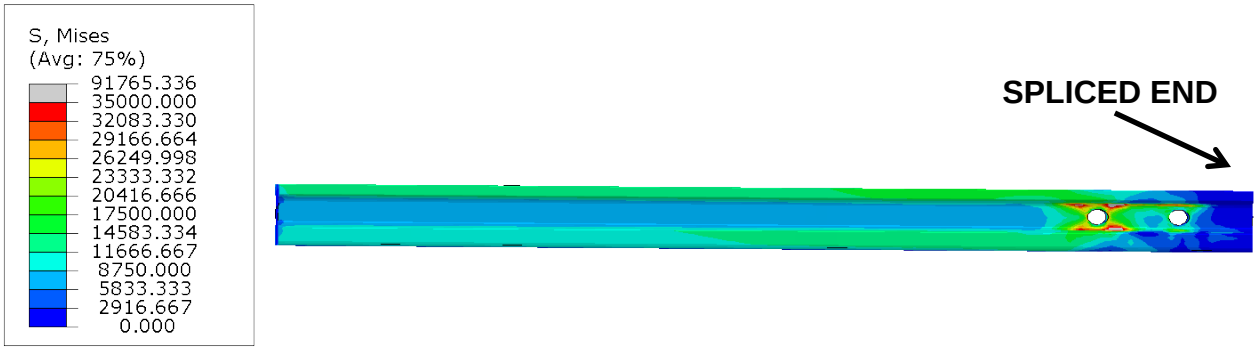

Figure 56. Mises stress distribution in the rail, out-of-plane bending step, high axial load case.